

Jefferson Lab PAC 44

# Nuclear Exclusive and Semi-inclusive Measurements with a New CLAS12 Low Energy Recoil Tracker

ALERT Run Group<sup>†</sup>

## EXECUTIVE SUMMARY

In this run group, we propose a comprehensive physics program to investigate the fundamental structure of the  ${}^4\text{He}$  nucleus. An important focus of this program is the study of the partonic structure of bound nucleons. To this end, we propose next generation nuclear measurements in which low energy recoil nuclei are detected. Tagging of recoil nuclei in deep inelastic reactions is a powerful technique that will provide unique information about the nature of medium modifications, through the measurement of the EMC ratio and its dependence on the nucleon off-shellness. Other important channels are the coherent exclusive Deep Virtual Compton Scattering (DVCS) and Deep Virtual Meson Production (DVMP) with a focus on the  $\phi$  meson. These are particularly powerful tools enabling model-independent nuclear 3D tomography through the access of partons' position in the transverse plane. These exclusive measurements will also be used to study the generalized EMC effect and for the first time access the gluonic tomography of nuclei via exclusive  $\phi$  electroproduction channel. Finally, we propose to measure tagged DVCS on light nuclei (d,  ${}^4\text{He}$ ) to extract both quasi-free neutron and bound neutron and proton Generalized Parton Distributions (GPDs). In both cases, the objective is to study nuclear effects and their manifestation in GPDs including the effect of final state interactions in the measurements of the bound nucleon beam spin asymmetries and the EMC ratio.

At the heart of this program is the Low Energy Recoil Tracker (ALERT) combined with the CLAS12 detector. The ALERT detector is composed of a stereo drift chamber for track reconstruction and an array of scintillators for particle identification. Coupling these two types of fast detectors will allow ALERT to be included in the trigger for efficient background rejection, while keeping the material budget as low as possible for low energy particle

---

<sup>†</sup>Contact Person: Kawtar Hafidi (kawtar@anl.gov)

detection. ALERT will be installed inside the solenoid magnet instead of the CLAS12 Silicon Vertex Tracker. We will use an 11 GeV longitudinally polarized electron beam (80% polarization) of 150 nA on a gas target straw filled with deuterium or  $^4\text{He}$  at 3 atm to obtain a luminosity of  $3.10^{34} \text{ cm}^{-2}\text{s}^{-1}$ . In addition we will need to run hydrogen and  $^4\text{He}$  targets at different beam energies for detector calibration. The following table summarizes our beam time request:

Measurements	Particles detected	Targets	Beam time request	Luminosity*
<b>ALERT Commissioning</b>	p, d, $^4\text{He}$	H and He	5 days	Various
<b>Tagged EMC</b>	p, $^3\text{H}$ , $^3\text{He}$	$^2\text{H}$ and He	20 + 20 days	$3.10^{34} \text{ cm}^{-2}\text{s}^{-1}$
<b>Tagged DVCS</b>	p, $^3\text{H}$ , $^3\text{He}$	$^2\text{H}$ and He	20 + 20 days	$3.10^{34} \text{ cm}^{-2}\text{s}^{-1}$
<b>Nuclear GPDs</b>	$^4\text{He}$	He	extra 10 days on He	$6.10^{34} \text{ cm}^{-2}\text{s}^{-1}$
<b>Additional Topics</b>	p, d, $^3\text{H}$ , $^3\text{He}$	$^2\text{H}$ and He	20 + 20 + (10) days	$3(6).10^{34} \text{ cm}^{-2}\text{s}^{-1}$
<b>TOTAL</b>			<b>55 days</b>	

---

\*This luminosity value is based on the effective part of the target. When accounting for the target's windows, which are outside of the ALERT detector, it is increased by 60%

# Tagged EMC Measurements on Light Nuclei

W.R. Armstrong, J Arrington, I. Cloet, K. Hafidi<sup>†</sup>, M. Hattawy, D. Potteveld, P. Reimer,  
Z. Yi

*Argonne National Laboratory, Lemont, IL 60439, USA*

J. Ball, M. Defurne, M. Garçon, H. Moutarde, S. Procureur, F. Sabatié  
*CEA, Centre de Saclay, Irfu/Service de Physique Nucléaire, 91191 Gif-sur-Yvette, France*

W. Cosyn

*Department of Physics and Astronomy, Proeftuinstraat 86, Ghent University, 9000 Ghent,  
Belgium*

M. Mazouz

*Faculté des Sciences de Monastir, 5000 Tunisia*

A. Accardi

*Hampton University, Hampton, VA 23668, USA*

J. Bettane, G. Charles<sup>†</sup>, R. Dupré<sup>†‡</sup>, M. Guidal, D. Marchand, C. Muñoz, S. Niccolai,  
E. Voutier

*Institut de Physique Nucléaire, CNRS-IN2P3, Univ. Paris-Sud, Université Paris-Saclay,  
91406 Orsay Cedex, France*

K. P. Adhikari, J. A. Dunne, D. Dutta, L. El Fassi, L. Ye

*Mississippi State University, Mississippi State, MS 39762, USA*

M. Amaryan, G. Dodge<sup>†</sup>

*Old Dominion University, Norfolk, VA 23529, USA*

V. Guzey

---

<sup>†</sup>Spokesperson

<sup>‡</sup>Contact person: dupre@ipno.in2p3.fr

*Petersburg Nuclear Physics Institute, National Research Center "Kurchatov Institute",  
Gatchina, 188300, Russia*

N. Baltzell<sup>†</sup>, C. Keppel, S. Stepanyan  
*Thomas Jefferson National Accelerator Facility, Newport News, VA 23606, USA*

S. Joosten, Z. E. Meziani, M. Paolone  
*Temple University, Philadelphia, PA 19122, USA*

F. Cao, K. Joo, A. Kim, N. Markov  
*University of Connecticut, Storrs, CT 06269, USA*

C. Ciofi degli Atti, S. Scopetta  
*Università di Perugia, INFN, Italy*

W. Brooks, A. El-Alaoui  
*Universidad Técnica Federico Santa María, Valparaíso, Chile*

S. Liuti  
*University of Virginia, Charlottesville, VA 22903, USA*

## **a CLAS Collaboration Proposal**

## Abstract

We propose to measure tagged deep inelastic scattering from light nuclei (deuterium and  $^4\text{He}$ ) by detecting the low energy nuclear spectator recoil (p,  $^3\text{H}$  and  $^3\text{He}$ ) in addition to the scattered electron. The proposed experiment will provide stringent tests leading to clear differentiation between the many models describing the EMC effect, by accessing the bound nucleon virtuality through its initial momentum at the point of interaction. Indeed, conventional nuclear physics explanations of the EMC effect mainly based on Fermi motion and binding effects yield very different predictions than more exotic scenarios, where bound nucleons basically lose their identity when embedded in the nuclear medium. By distinguishing events where the interacting nucleon was slow, as described by a mean field scenario, or fast, very likely belonging to a correlated pair, will clearly indicate which phenomenon is relevant to explain the EMC effect. An important challenge for such measurements using nuclear spectators is the control of the theoretical framework and, in particular, final state interactions. This experiment will directly provide the necessary data needed to test our understanding of spectator tagging and final state interactions in  $^2\text{H}$  and  $^4\text{He}$  and their impact on the semi-inclusive measurements of the EMC effect described above.

# Contents

<b>Abstract</b>	<b>5</b>
<b>Introduction</b>	<b>8</b>
<b>1 The EMC effect in SIDIS</b>	<b>12</b>
1.1 The spectator mechanism . . . . .	12
1.2 EMC effect in deuteron . . . . .	14
1.3 EMC effect in helium . . . . .	15
1.4 Tagged EMC ratio . . . . .	16
1.5 Flavor dependent parton distribution functions . . . . .	18
1.6 Summary . . . . .	18
<b>2 Experimental Setup</b>	<b>20</b>
2.1 The CLAS12 Forward Detector . . . . .	20
2.2 Design of the ALERT Detector . . . . .	22
2.2.1 The Drift Chamber . . . . .	23
2.2.2 The scintillator array . . . . .	26
2.3 Reconstruction . . . . .	29
2.3.1 Track Fitting . . . . .	30
2.3.2 Track Reconstruction and Particle Identification . . . . .	31
2.4 Drift chamber prototype . . . . .	34
2.5 Other options for a Low Energy Recoil Detector . . . . .	35
2.5.1 Central Detector . . . . .	36
2.5.2 BoNuS12 Radial Time Projection Chamber . . . . .	37
2.5.3 Summary . . . . .	38
2.6 Technical contributions from the research groups . . . . .	39
2.6.1 Argonne National Laboratory and Temple University . . . . .	39
2.6.2 Institut de Physique Nucléaire d’Orsay . . . . .	39
2.6.3 Jefferson Laboratory . . . . .	40

---

<b>3 Proposed Measurements</b>	<b>41</b>
3.0.4 Monte-Carlo Simulation . . . . .	41
3.0.5 Beam Time Request . . . . .	42
3.1 Projections . . . . .	42
3.1.1 Testing the Spectator Model . . . . .	43
3.1.2 EMC effect in deuterium . . . . .	44
3.1.3 Testing the Rescaling Models . . . . .	44
3.1.4 Tagged EMC Ratio . . . . .	45
3.1.5 The Flavor Dependent Nuclear Effects . . . . .	47
<b>Summary and Beam Time Request</b>	<b>48</b>
Relation to other proposals . . . . .	48

# Introduction

Inclusive electron scattering is a simple and yet a powerful tool to probe the structure of the nucleus; in the Deep Inelastic Scattering (DIS) regime it allows to access the partonic structure of hadrons. Using the nucleus as a target permits to study how nucleons and their parton distributions are modified when embedded in the nuclear environment. The modification of quark distributions in bound nucleons was first observed through the modification of the per-nucleon cross section in nuclei, known as the "EMC effect" [1]. For moderate Bjorken  $x$ ,  $0.35 \leq x_B \leq 0.7$ , the per-nucleon DIS structure function for nuclei with  $A \geq 3$  was found to be suppressed compared to that of deuterium, the historic measurement being confirmed and refined in the past 30 years [2, 3, 4, 5, 6, 7].

Since its discovery, the EMC effect has been a subject of extensive theoretical investigations aimed at understanding its underlying physics. While progress has been made in interpreting the main features of the effect, no single model has been able to explain convincingly the effect for both its  $x_B$  and  $A$  dependencies [8, 9, 10]. A unifying understanding of the physical picture is still under intense debate. Most models of the EMC effect can be classified into two main categories:

- "Conventional" nuclear models [11, 12, 13, 14] in which the effect could be understood by a reduced effective nucleon mass due to the nuclear binding, causing a shift of  $x_B$  to higher values ( $x_B$ -rescaling or binding models). In these models the mass shift is sometimes accompanied by an increased density of virtual pions associated with the nuclear force (pion cloud models).
- Models involving the change of the quark confinement size in the nuclear medium [15, 16, 17, 18] can be viewed, in the language of QCD, as  $Q^2$  rescaling models. In some cases, a simple increase of the nucleon radius is assumed (nucleon swelling), while in others, quark deconfinement is invoked and the nucleon degrees of freedom are replaced by multi-quark clusters.
- Some more elaborate models fall in between or give very different predictions. We note here in particular the Point Like Configurations (PLC) suppression model as it gives direct predictions as a function of the nucleon off-shellness. It was argued in [19] that PLCs are suppressed in bound nucleons and that large  $x_B$  configurations in nucleons have smaller than average size leading to the EMC effect at large  $x_B$ . The EMC effect



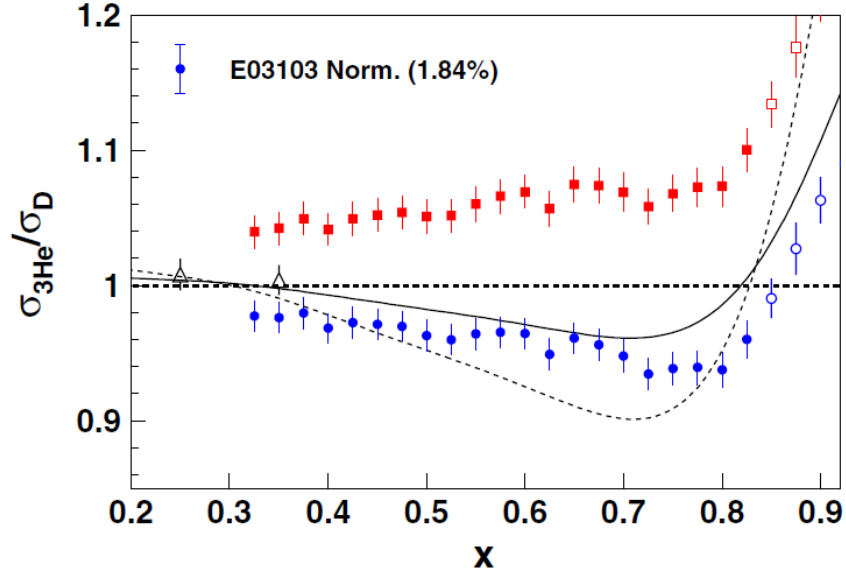


Figure 1: EMC ratio  ${}^3\text{He}$ , the upper squares are the raw  ${}^3\text{He}/{}^2\text{H}$  ratios, while the bottom circles show the isoscalar EMC ratio. The triangles are the HERMES results [20] which use a different isoscalar correction. The solid and dashed curves are the SLAC  $A$ -dependent fits to  ${}^3\text{He}$  and carbon, respectively [7].

in this model is predicted to be proportional to the off-shellness of the struck nucleon and hence dominated by the contribution of the short-range correlations.

Recent experiment at Jefferson Lab measured the EMC effect for a series of light nuclei [7]. Fig. 1 shows the first measurements of the EMC effect for  ${}^3\text{He}$  at large  $x_B$ , which was found to be roughly one third of the effect observed in  ${}^4\text{He}$ , violating the  $A$ -dependent fit to the SLAC data. In the same way, the large EMC effect found in  ${}^9\text{Be}$  contradicts a simple density-dependent behavior (Fig. 2). This suggests that the EMC effect may be sensitive to the local density or details of the nuclear structure, which has been first introduced in [21]. Other models have also predicted a local EMC effect and describe the modification of the nucleons depending on their shells [22, 23, 24]. The possibility of the EMC effect depending on the local environment of the nucleon also motivates the investigation of possible connections between the EMC effect and other density-dependent effects such as short-range correlations [25, 26]. Short-range correlations (SRC) occur between nucleons located at less than the average inter-nucleon distance with high relative momentum [27, 28, 29]. Those pairs of nucleons carry 80% of all nucleons kinetic energy inside the nucleus although they only represent about 20% of the total number of nucleons [30]. The plateau obtained in the inclusive cross section ratios of two nuclei (for example iron and deuterium) in the region  $x_B > 1.5$  for  $Q^2 > 1.5 \text{ GeV}^2$  indicates that for nucleon momentum larger than Fermi momentum ( $p \geq p_N \simeq 275 \text{ MeV}/c$ ), the nucleon momentum distributions in different

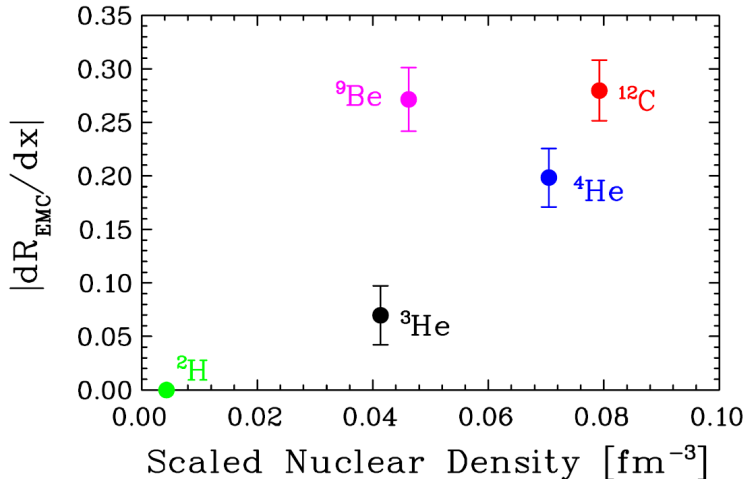


Figure 2: The slope of the isoscalar EMC ratio for  $0.35 < x_B < 0.7$  as a function of nuclear density [7].

nuclei have similar shapes but differ in magnitude. The ratio of the cross sections in the plateau region also called the "SRC scale factor  $a_{2N}(A/d)$ " was found to be linearly correlated with the slope of the EMC effect [26]. This striking correlation shown in Fig. 3 could indicate that high momentum bound nucleons are important players in the EMC effect.

To investigate the matter further, it is important to study the EMC effect as a function of both  $x_B$  and the nucleon off-shellness, by measuring the recoil fragment in addition to the scattered electron as is developed in this proposal (the relation between spectator momentum and off-shellness has been studied in detail in [31]). The two main challenges to perform such a measurement are, first, to be able to detect the low energy nuclear fragments and, second, to understand the Final State Interaction (FSI) effects on the observables.

The recent development of two small radial time projection chambers (RTPC) by the CLAS collaboration for the measurement of the structure function of the neutron, by tagging the spectator proton from a deuterium target [32], and the measurement of coherent deep virtual Compton scattering off <sup>4</sup>He [33] has raised a lot of interest to use the same detector for this proposed tagged EMC measurement. However, it was found that the particle identification capabilities of the RTPC are not good enough to properly distinguish the different nuclear isotopes measured (in particular <sup>3</sup>H from <sup>3</sup>He). Therefore, we propose to use a different detector (a Low Energy Recoil Tracker - ALERT) based on a low gain drift chamber and a scintillator array for time of flight measurements. Such a detector appears to be perfectly suited for our measurement as it offers low energy and large angle capabilities to measure slow recoils similar to the RTPC. Moreover, such a detector will be much faster to collect the deposited charges making it possible to include it in the trigger. This will

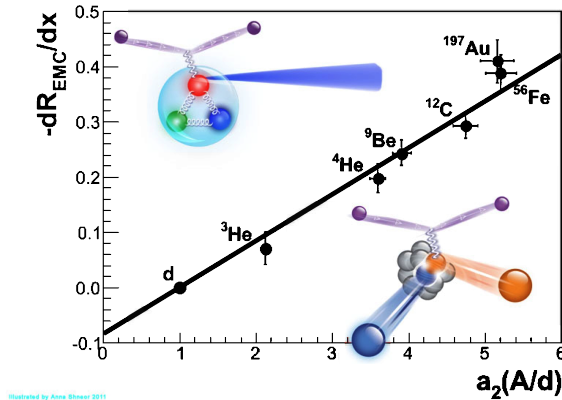


Figure 3: The EMC slopes versus the SRC scale factors. The uncertainties include both statistical and systematic errors added in quadrature.

allow to reject the overwhelming majority of the events ( $\sim 90\%$ ) where the nuclear recoil does not make it into the detection area.

Another important challenge for tagged measurements is to control the impact of FSI on the observables. The large acceptance of both CLAS12 and ALERT is very important in this regard as it allows to measure at the same time the regions of the phase space expected to have negligible FSI and the regions where we expect a larger FSI effect. The models used to correct for FSI [34, 35, 36, 37] can therefore be tested in a wide kinematic range in the exact same conditions as the main measurement in order to ensure that the effect is understood properly. Then with the application of cuts to select the region where the effect is small, we can reduce the impact of FSI to a minimum. This procedure allows to make sure FSI effects are small and under control to minimize systematic uncertainty on our observables.

# Chapter 1

## The EMC effect in SIDIS

At this point, it became clear that in order to advance our understanding of the EMC effect, it is necessary to study new observables such as the nucleon off-shellness which can be accessible in semi inclusive measurements. Interests for slow nucleons and fragments tagging ( $e+A \rightarrow e'+N+X$ ) studies are older than the EMC effect itself and has been identified earlier to be a promising tool to study nuclear effects [21, 38, 39]. In more recent work, Melnitchouk *et al.* [40] showed that the tagged structure functions of deuteron in ( $e, e'N_s$ ) semi-inclusive reactions, where  $N_s$  denotes the spectator nucleon, is a sensitive probe of the modification of the intrinsic structure of the bound nucleon allowing to discriminate between different EMC models. The extended case to heavier nuclei  $A$ , where the recoil nucleus ( $A - 1$ ) is tagged was developed by Ciofi degli Atti *et al.* [24, 37, 41, 42], demonstrating the importance of such measurements in the understanding the EMC-type effects. In this proposal, we want to test experimentally the validity of the spectator mechanism to investigate the origin of the medium induced modification of the nucleon structure function through several observables based on tagged DIS off deuterium and helium targets.

### 1.1 The spectator mechanism

In the spectator mechanism or plane wave impulse approximation (PWIA), the DIS process corresponds to the absorption of the virtual photon by a quark inside a nucleon, followed by the recoil of the spectator nucleus  $A - 1$  without any final state interaction (Fig. 1.1). The differential semi-inclusive cross section can be written as [24]

$$\sigma_1^A(x_B, Q^2, \vec{P}_{A-1}, y_A, z_1^A) = \frac{d^4\sigma}{dx dQ^2 d\vec{P}_{A-1}} = K^A(x, y_A, Q^2, z_1^A) n_A(|\vec{P}_{A-1}|) z_1^A F_2^{N/A}(x_A, Q^2, p_1^2), \quad (1.1)$$

where  $Q^2 = -q^2 = -(k_e - k'_e)^2 = \vec{q}^2 - \nu$  is the four-momentum transfer, with  $\vec{q} = \vec{k}_e - \vec{k}'_e$  and  $\nu = E_e - E'_e$ ,  $x_B = Q^2/2M\nu$  is the Bjorken scaling variable,  $p_1 \equiv (p_{10}, \vec{p}_1)$ , with  $\vec{p}_1 \equiv -\vec{P}_{A-1}$ , is the four-momentum of the off-shell nucleon before its interaction with the virtual photon.

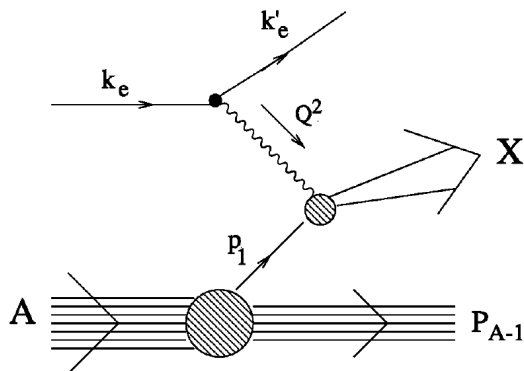


Figure 1.1: The process  $A(e, e'(A-1))X$  within the impulse approximation [24].

$F_2^{N/A}$  is the DIS structure function of the nucleon  $N$  in the nucleus  $A$ ,  $n_A(|\vec{P}_{A-1}|)$  is the three-momentum distribution of the bound nucleon,  $z_1^A = (p_1 \cdot q)/M\nu$  is the light cone momentum of the bound nucleon and  $K^A$  is a kinematical factor given by

$$K^A(x_B, y_A, Q^2, z_1^A) = \frac{4\pi\alpha^2}{Q^4 x_B} \cdot \left(\frac{y}{y_A}\right)^2 \times \left(\frac{y_A^2}{2} + (1 - y_A) - \frac{p_1^2 x_B^2 y_A^2}{(z_1^A)^2 Q^2}\right), \quad (1.2)$$

with  $y = \nu/E_e$ ,  $y_A = (p_1 \cdot q)/(p_1 \cdot k_e)$  and  $x_A = x_B/z_1^A$ .

Nuclear effects in Eq. 1.1 are generated by the nucleon momentum distribution  $n_A(|\vec{P}_{A-1}|)$  and by the quantities  $y_A$  and  $z_1^A$ , which differ from the corresponding quantities for a free nucleon ( $y = \nu/E_e$  and  $z_1^N = 1$ ). In this framework the off-mass shellness of the nucleon ( $p_1^2 \neq M^2$ ) generated by nuclear binding is taken into account within some small relativistic corrections when  $A > 2$  [43]. In all the studies we propose here, as well as in proposals such as [44, 45, 46], it is important to ensure that the spectator mechanism is working and that rescattering with spectator nucleons is properly modeled. Our main goal here is to make sure we understand deuterium and the extension of the formalism to the helium target. To test the spectator mechanism, we use the  $\vec{P}_{A-1}$  dependence of semi-inclusive cross section ratio of different nuclei at the same values of  $x_B$ ,  $Q^2$  and with  $|\vec{P}_{A'-1}| = |\vec{P}_{A-1}|$

$$R(x_B, Q^2, |\vec{P}_{A-1}|, z_1^A, z_1^{A'}, y_A, y_{A'}) \equiv \frac{\sigma_1^A(x_B, Q^2, |\vec{P}_{A-1}|, z_1^A, y_A)}{\sigma_1^{A'}(x_B, Q^2, |\vec{P}_{A'-1}|, z_1^{A'}, y_{A'})}. \quad (1.3)$$

In the Bjorken limit, the  $A$  dependence of  $R$  is expected to be entirely dominated by the  $A$  dependence of the nucleon momentum distribution  $n_A(|\vec{P}_{A-1}|)$ , which exhibits a strong  $A$  dependence at low recoil momentum region. Therefore, measurements of the  $R$  ratio as a function of the recoil momentum  $|\vec{P}_{A-1}|$  provide a stringent test for the spectator mechanism independently of the model for  $F_2^{N/A}$ . Fig. 1.2 illustrates the expected behavior of the ratio

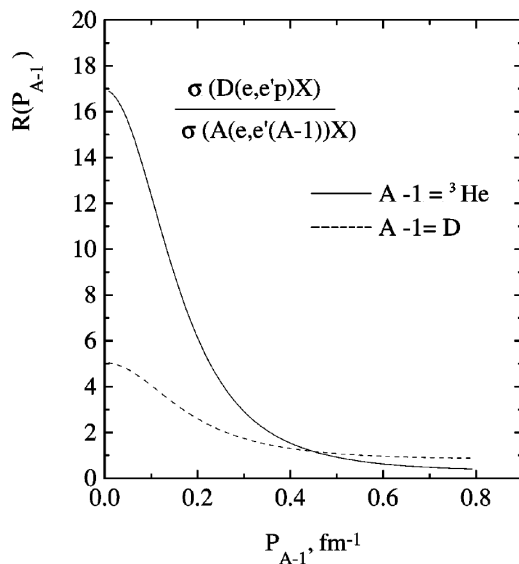


Figure 1.2: The ratio  $R(A, A', |\vec{P}_{A-1}|)$  for the targets  ${}^3\text{H}$  (dashed) and  ${}^4\text{He}$  (full) as a function of the momentum of the backward emitted nucleus [24] relative to the virtual photon direction.

in Eq. 1.3 from the processes  $\text{D}(e, e'p)X$ ,  ${}^3\text{He}(e, e'D)X$  and  ${}^4\text{He}(e, e'{}^3\text{He})X$ , as deep inelastic scattering off a bound neutron in different nuclei. From the previous discussion, it is clear that the observation of recoiling nuclei in the ground state, with a  $|\vec{P}_{A-1}|$ -dependence similar to the one predicted by the momentum distributions, would represent a stringent check of the spectator mechanism, which, in turns, would indicate the absence of significant FSI between the electroproduced hadronic states and the nuclear medium. Detailed studies [34, 35, 36, 37, 40, 47, 48] have shown that the FSI effects are minimized in the backward recoiling angle relative to the virtual photon direction and maximized in perpendicular kinematics. The detection of the ground or low energy excited states of the  $(A - 1)$  recoil would represent a strong indication that the hadronization length is larger than the effective nuclear dimension, since if the struck quark hadronizes inside the nucleus, it will likely result in breaking up the nucleus.

## 1.2 EMC effect in deuteron

Recent work from Griffioen *et al.* [49] has shown that the EMC effect is present, but very small, in the deuteron. However, the recent finding of the possible dependence of the EMC effect on local nuclear density raised the interest in using spectator nucleons to study the EMC effect. Indeed, the momentum of the spectator nucleon can be directly linked to the distance between the two nucleons in the deuteron [43] and therefore results in the

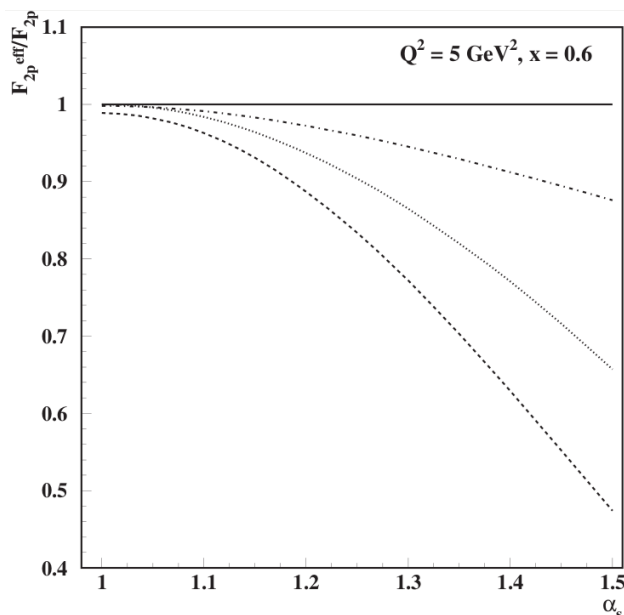


Figure 1.3:  $F_{2p}^{eff}$  as a function of  $\alpha_s$  for  $x = 0.6$  and  $p_T = 0$ . Dashed line is a prediction for the PLC suppression model, dotted is for the  $Q^2$ -rescaling model, and dot-dashed for the binding/off-shell model [40].

enhancement of the EMC effect in certain configurations.

Melnitchouk *et al.* [40] use the ratio of the effective  $F_{2p}^{eff}$  measured in the deuterium, tagging the neutron, and compare it to the usual free  $F_{2p}$ . They predict significant effects for various models as a function of  $\alpha \equiv \frac{E_s - p_z^s}{M}$  (with  $E_s$  and  $p_z^s$  the energy and longitudinal momentum of the spectator, respectively, and  $M$  its mass), which characterizes the nucleon off-shellness. A semi-inclusive measurement will allow to discriminate between the very different model predictions (Fig. 1.3).

### 1.3 EMC effect in helium

The process described for deuterium can be easily extended to heavier nuclei with several advantages. First, the nuclear effects in light nuclei, such as  ${}^4\text{He}$ , are much stronger, thus it enhances significantly the cross section for events with spectator momentum  $\gtrsim 250$  MeV. Second, by detecting an intact light nucleus ( ${}^3\text{H}$  or  ${}^3\text{He}$ ), we ensure that the final state interaction with the spectator is small and the contributions from the current or target fragmentation of the hard process are suppressed. On the down side, the theoretical calculations are more difficult, however recent theoretical progress indicates that these

calculations although tedious could be performed [34, 36, 37, 39, 43].

The quantity  $R^A$  which is defined by:

$$R^A(x_B, x'_B, Q^2, |\vec{P}_{A-1}|) \equiv \frac{\sigma_1^A(x_B, Q^2, |\vec{P}_{A-1}|, z_1^{(A)}, y_A)}{\sigma_1^A(x'_B, Q^2, |\vec{P}_{A-1}|, z_1^{(A)}, y_A)}, \quad (1.4)$$

represents the ratio between the cross sections on the nucleus  $A$  at two different values of the Bjorken scaling variable. Due to the cancellation of all the other terms but the nucleon structure functions in Eq. 1.4,  $R^A$  is highly sensitive to the nuclear effect. In the binding model ( $x$ -rescaling), where the inclusive nuclear structure function is expressed through a convolution of the nuclear spectral function and the structure function of the bound nucleon, one has

$$R^A(x_B, x'_B, Q^2, |\vec{P}_{A-1}|) = \frac{x'_B F_2^{N/A}(\frac{x_B}{z_1^A}, Q^2)}{x_B F_2^{N/A}(\frac{x'_B}{z_1^A}, Q^2)}. \quad (1.5)$$

In the  $Q^2$ -rescaling model [18], which is based on the medium modification of the  $Q^2$ -evolution equations of QCD and the assumption that the quark confinement radius for a bound nucleon is larger than the one for a free nucleon, the ratio becomes

$$R^A(x_B, x'_B, Q^2, |\vec{P}_{A-1}|) = \frac{x'_B F_2^{N/A}(x_B, \xi_A(Q^2)Q^2)}{x_B F_2^{N/A}(x'_B, \xi_A(Q^2)Q^2)} \quad (1.6)$$

While Eq. 1.5 is expected to depend both on  $A$  and  $|\vec{P}_{A-1}|$ , Eq. 1.6 would be a constant. By detecting nuclei with different recoil angles, this ratio would exhibit different behaviors, allowing a more detailed examination of the dynamics. Fig. 1.4 shows theoretical predictions of the  $R^A$  ratio in the  $x$ - and  $Q^2$ -rescaling models at both perpendicular and backward recoil kinematics.

## 1.4 Tagged EMC ratio

Another observable used in theoretical calculations for the tagged EMC ratio is

$$R_0(x, Q^2) = \frac{\int_a^b \sigma_1^A d\vec{P}_{A-1}}{\int_a^b \sigma_1^D d\vec{P}_{A-1}}, \quad (1.7)$$

in which the cross section is integrated over a small momentum range of the recoil nucleus  $\vec{P}_{A-1}$ . In binding models it leads to opposite behavior for recoil nuclei emitted forward versus backward (Fig. 1.5) that cancels in the usual inclusive EMC ratio. These resulting deviations are much larger than the usual inclusive EMC effect and provides opportunity for a significant experimental test of the binding models.



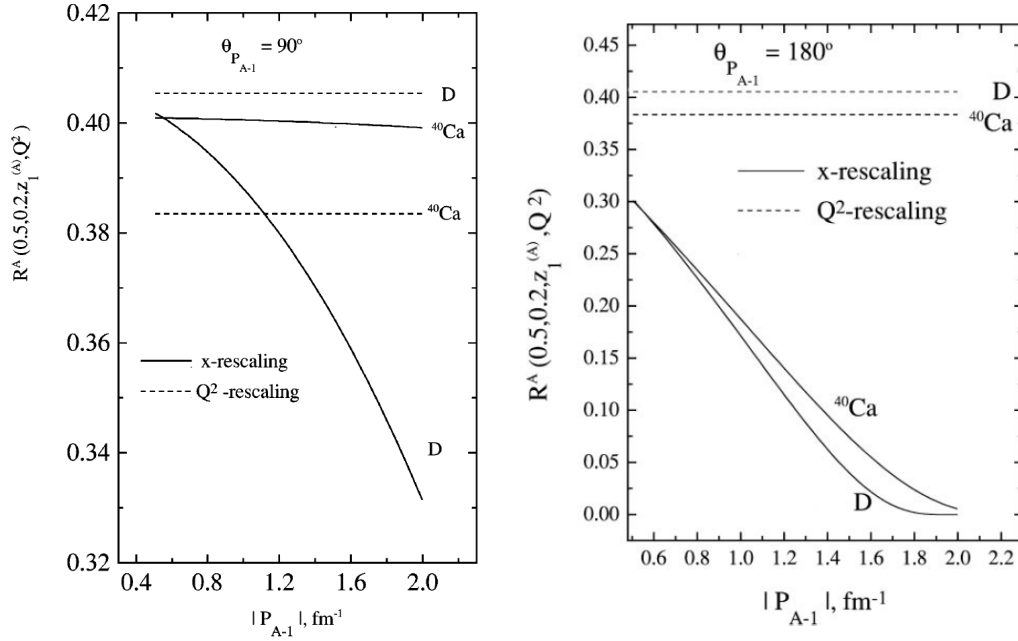


Figure 1.4: The ratio  $R^A(x_B, x'_B)$  for  $A = 2$  and  $A = 40$ ,  $x_B = 0.2$  and  $x'_B = 0.5$ ,  $Q^2 = 20$   $\text{GeV}/c$ , plotted versus the momentum of the recoil nucleus ( $A - 1$ ) at perpendicular (left) and backward (right) angle ( $\theta_{P_{A-1}} = 180^\circ$ ). The full and dashed curves are predictions of the  $x_B$ -rescaling (binding) and  $Q^2$ -rescaling models, respectively.

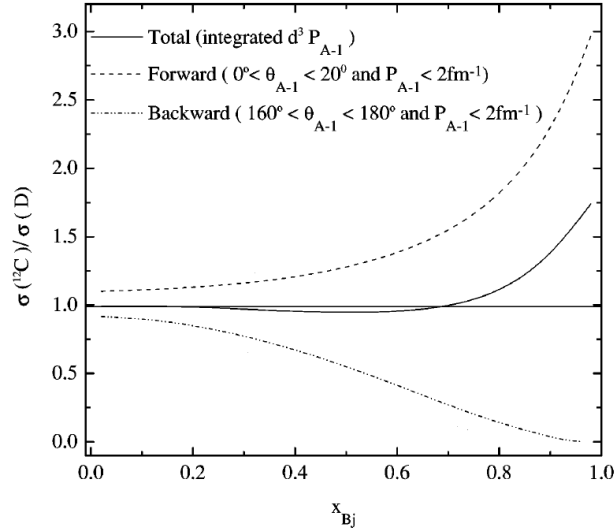


Figure 1.5: The semi-inclusive EMC ratio  $R_0(x, Q^2)$  versus  $x$  with nuclei emitted forward and backward, the full curve is the usual inclusive EMC ratio, the dashed and dotted curves are predictions for the local EMC effect for different spectator recoil angles [24] (see the legend).

## 1.5 Flavor dependent parton distribution functions

Measurements of tagged structure functions have been carried out in CLAS by the e6 run group to study the EMC effect in deuteron [47] and later by the BoNuS collaboration [50] to extract the  $F_2^n$  structure function by tagging the low momentum recoil proton. The main goal of the BoNuS measurements was to extract the ratio  $F_2^n/F_2^p$  at high  $x_B$  and therefore access the ratio of down to up quark distribution ( $d/u$ ) [32] at high  $x_B$ . By using  $^4\text{He}$  targets and tagging the recoiling  $^3\text{He}$  and  $^3\text{H}$  nuclei, one can select scattering off a weakly or deeply bound neutron and proton respectively depending on their off-shellness in the  $^4\text{He}$  nucleus. Since bound neutrons are always off-shell, even when  $P_{3\text{He}} = 0$ , an extrapolation procedure is needed to extract the free (i.e. on-shell) neutron structure function from the tagged recoil data [51, 52]. One could measure the  $F_2$  structure functions of a weakly bound neutron in  $^4\text{He}$  and compare it to the  $^2\text{H}$  data to detect any nuclear dependence. This procedure is necessary for neutrons due to the absence of a free neutron target. It can also be quantitatively benchmarked using the  $^4\text{He}$  tagged data for scattering off a weakly bound proton, and comparing the results to the well measured free proton structure functions.

In addition, the ratio  $(F_2^n/F_2^p)^{\text{bound}} / (F_2^n/F_2^p)^{\text{free}}$  can be measured to extract the distributions of  $d/u$  in a free nucleon and compare it to the same ratio for bound nucleon. This is one way to explore the flavor dependent nuclear parton distributions which are little known experimentally. Such an effect, either in the anti-shadowing or EMC region, has been widely used to explain the NuTeV anomaly [53, 54].

## 1.6 Summary

In this chapter, we have shown very strong theoretical motivations to measure the tagged structure function of nucleons in light nuclei such as deuterium and helium. The main difficulty being to properly handle the FSI. To solve this challenge, a large acceptance detector is necessary in order to demonstrate that data match models on a wide kinematic range in angle and momentum. Moreover, such large acceptance detector needs to work at the lowest possible energy to ensure that quasi-free nucleons of low off-shellness can be effectively compared with the more virtual ones. Our proposition for such a detector is presented in the next chapter.

We presented theoretical work suggesting that a measurement on deuterium will already show an effect, however we have also showed that higher nuclear masses provide much stronger signals and would ensure a compelling measurement. Observing several nuclei in different kinematics lead to very different results for the classic pure  $x_{Bj}$  and  $Q^2$ -rescaling models. This will allow us to determine precisely which picture or which combination of the two pictures is at the origin of the EMC effect. This measurement will therefore provide a completely new insight into the origin of the EMC effect and provide clear guidelines to build new models and better understanding of the partonic structure of nuclei.

In addition, our proposed experiment will allow to test the flavor symmetry of the nuclear effects, which have been discussed by theoretical predictions in the anti-shadowing and EMC regions. While this experiment is not dedicated to this question, for which additional isospin asymmetric targets would be necessary, we show that it can already provide a first test and pave the way for future works.

# Chapter 2

## Experimental Setup

The different measurements of the ALERT run group require large kinematic coverage and the ability to identify the different nuclear species properly. The CLAS12 detector augmented by a low energy recoil detector is key for the success of such measurements. We summarize in Table 2.1 the requirements for the different experiments proposed in the run group.

This chapter will begin with a description of CLAS12 and the ALERT detector. After presenting the details of this new detector system, we will present an overview of the BoNuS12 RTPC followed by a discussion of how already approved or existing detectors do not satisfy the requirements for our run group.

Measurement	Particles detected	$p_{threshold}$	$\theta_{max}$
Tagged EMC	p, $^3\text{H}$ , $^3\text{He}$	As low as possible	As close to $\pi$ as possible
Tagged DVCS	p, $^3\text{H}$ , $^3\text{He}$	As low as possible	As close to $\pi$ as possible
Nuclear GPDs	$^4\text{He}$	$230 < p < 400 \text{ MeV}/c$	$\pi/4 < \theta < \pi/2$ rad

Table 2.1: Requirements for the detection of low momentum spectators fragments of the proposed measurements.

### 2.1 The CLAS12 Forward Detector

The CLAS12 detector is designed to operate with 11 GeV beam at an electron-nucleon luminosity of  $\mathcal{L} = 1 \times 10^{35} \text{ cm}^{-2}\text{s}^{-1}$ . The baseline configuration of the CLAS12 detector consists of the Forward Detector and the Central Detector packages [55] (see Fig. 2.1).

The scattered electrons will be detected in the forward detector which consists of the High Threshold Cherenkov Counters (HTCC), Drift Chambers (DC), the Low Threshold

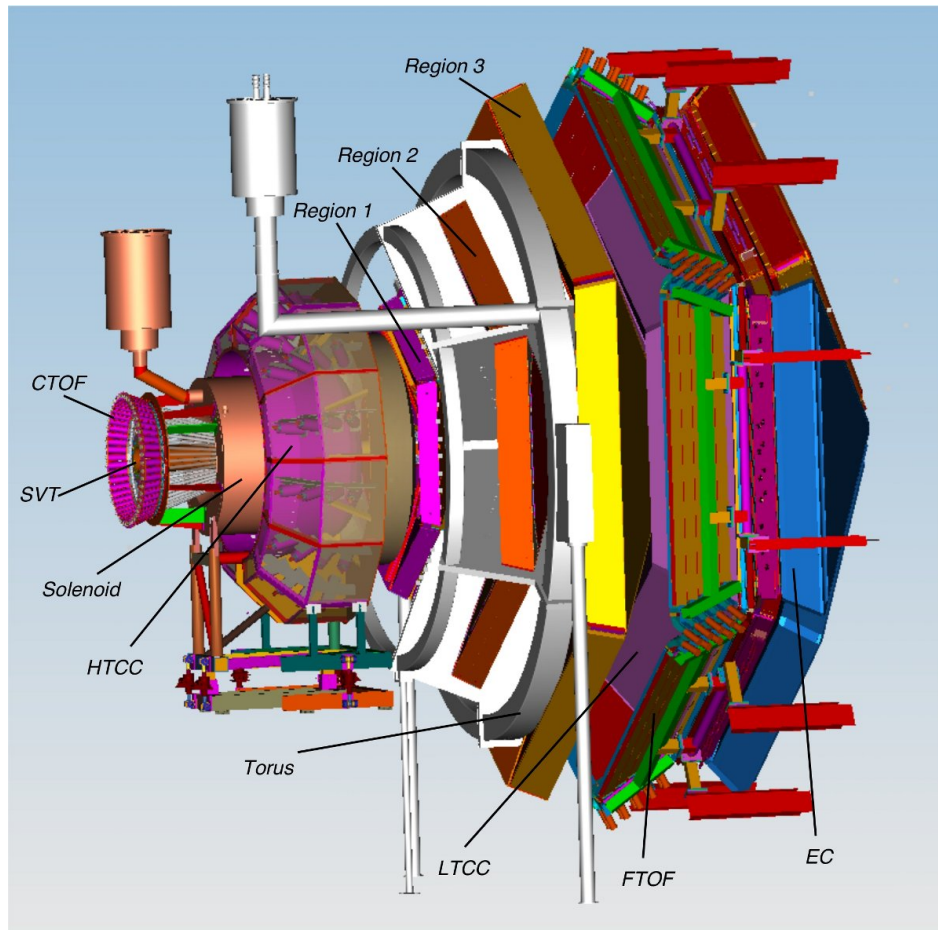


Figure 2.1: The schematic layout of the CLAS12 baseline design.

Cherenkov Counters (LTCC), the Time-of-Flight scintillators (TOF), the Forward Calorimeter and the Preshower Calorimeter. The charged particle identification in the forward detector is achieved by utilizing the combination of the HTCC, LTCC and TOF arrays with the tracking information from the Drift Chambers. The HTCC together with the Forward Calorimeter and the Preshower Calorimeter will provide a pion rejection factor of more than 2000 up to a momentum of 4.9 GeV, and a rejection factor of 100 above 4.9 GeV/c.

## 2.2 Design of the ALERT Detector

We propose to build a low energy recoil detector consisting of two sub-systems: a drift chamber and a scintillator hodoscope. The drift chamber will be composed of 8 layers of sense wires to provide track information while the scintillators will primarily provide particle identification. To reduce the material budget, thus pushing the energy threshold for detecting recoil particles as low as possible, the scintillator hodoscope will be placed inside the chamber, just outside of the last layer of drift wires. The good time resolution, and therefore position resolution, of the drift chamber, when coupled with the scintillators, will provide energy loss, timing, and azimuthal angle measurements for a sizable fraction of recoil particles.

The drift chamber volume will be filled with a light gas mixture (90% He and 10% C<sub>4</sub>H<sub>10</sub>) in order to not be sensitive to relativistic particles (*i.e.* electrons, gammas) and neutron backgrounds. Furthermore, a light gas mixture will increase the drift speed of electrons created during the ionization. This allows the chamber to withstand higher rates due to a shorter hit occupancy time window. The gas will likely be at atmospheric pressure but we plan to evaluate the possibility of working at a lower pressure. Based on these characteristics, the signals from this chamber and the scintillators will be used as an independent trigger, thus, reducing the DAQ trigger rate and allowing for operation at increased luminosity.

The detector must be designed to fit inside the outermost layer of Micromegas; the silicon vertex tracker and the remaining layers of Micromegas will be removed. The available space has thus an outer radius of 20 cm. A schematic layout of the preliminary design is shown in Fig. 2.2. The different detection elements are all covering about 340° of the polar angle to leave room for mechanics, and are 30 cm long with an effort made to reduce the particle energy loss through the materials. It is composed of:

- a cylindrical target, that compared to the eg6 run, is longer ( $\sim 30$  cm), wider (outer radius is 6 mm) and operating with lower pressure ( $\sim 3$  atm) in order to use a thinner target wall ( $\sim 25\mu\text{m}$  Kapton) <sup>1</sup>;

<sup>1</sup>During the eg6 run, the pressure of the drift gas in the RTPC was  $\sim 1$  atm, and the pressure of the target was  $\sim 6.5$  atm. Recent tests from S. Christo (JLab) demonstrated the feasibility of a 3 atm target with a 30  $\mu\text{m}$  wall, including safety margins.

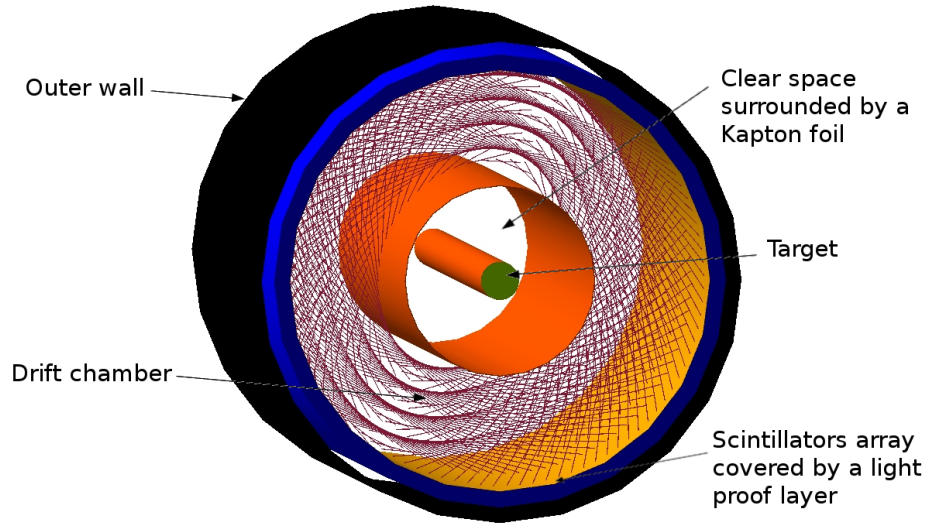


Figure 2.2: The schematic layout of the ALERT detector design, viewed from the beam direction.

- a clear space filled with helium to reduce secondary scattering from the high rate Moller electrons. Its outer radius is 30 mm;
- the drift chamber, its inner radius is 32 mm and its outer radius is 85 mm. It will detect the trajectory of the low energy nuclear recoils;
- two rings of plastic scintillators placed inside the gaseous chamber, with total thickness of roughly 20 mm.

### 2.2.1 The Drift Chamber

While drift chambers are very useful to cover large areas at a moderate price, huge progress has been made in terms of the ability to withstand higher rates using better electronics, shorter distance between wires and optimization of the electric field over pressure ratio. Our design is based on other chambers developed recently. For example for the dimuon arm of ALICE at CERN, drift chambers with cathode planes were built in Orsay [56]. The gap between sense wires is 2.1 mm and the distance between two cathode planes is also 2.1 mm, the wires are stretched over about 1 m. Belle II is building a cylindrical drift chamber very similar to what is needed for this experiment and for which the space between wires is around 2.5 mm [57]. Finally, a drift chamber with wire gaps of 1 mm is being built for the small wheel of ATLAS at CERN [58]. The cylindrical drift chamber proposed for our experiment is 300 mm long, and we therefore considered that a 2 mm gap between wires was technically a rather conservative goal. Optimization is

envisioned based on experience with prototypes.

The radial form of the detector does not allow for 90 degrees x-y wires in the chamber. Thus, the wires of each layer are at alternating angle of  $\pm 10^\circ$ , called the stereo-angle, from the axis of the drift chamber. We use stereo-angles between wires to determine the coordinate along the beam axis ( $z$ ). This setting makes it possible to use a very thin forward end-plate to reduce multiple scattering of the outgoing high-energy electrons. A rough estimate of the tension due to about 2600 of 30 cm long wires is under 600 kg, which appears to be reasonable for a composite endplate.

Our drift chamber cells are composed of one sense wire made of gold plated tungsten surrounded by field wires, however the presence of the 5 T magnetic field complicates the field lines. Several cell configurations have been studied with MAGBOLTZ [59] and will be tested in a prototype (see section 2.4). For now, we decided to choose a conservative configuration as shown in Fig. 2.3. The sense wire is surrounded by 6 field wires placed equidistantly from it in a hexagonal pattern. The distance between the sense and field wires is constant and equal to 2 mm. Two adjacent cells share the field wire placed between them. The current design will have 8 layers of cells of increasing radius. The simulation code MAGBOLTZ is calculating the drift speed and drift paths of the electrons (Fig. 2.3). With a moderate electric field, the drift speed is around 10 microns/ns, the average drift time expected is thus 250 ns (over 2 mm). Assuming a conservative 10 ns time resolution, the spatial resolution is expected to be around 200 microns due to field distortions and spread of the signal.

The maximum occupancy, shown in Fig. 2.4, is expected to be of 5% for the inner most wires at  $10^{35} \text{ cm}^{-2}\text{s}^{-1}$  (including the target windows). This is the maximum available luminosity for the baseline CLAS12 and is obtained based on the physics channels depicted in Fig. 2.5, assuming an integration time of 200 ns and considering a readout wire separation of 4 mm. This amount of accidental hits does not appear to be reasonable for a good tracking quality, we therefore decided to run only at half this luminosity for our main production run. This will keep occupancy below 3%, which is a reasonable amount for a drift chamber to maintain high tracking efficiency. When running the coherent processes with the  $^4\text{He}$  target, it is not necessary to detect the protons<sup>2</sup>, and the rate of accidental hits can then be highly reduced by increasing the detection threshold, thus making the chamber blind to protons<sup>3</sup>. In this configuration, considering that our main contribution to occupancy are quasi-elastic protons, we are confident that the ALERT can work properly at  $10^{35} \text{ cm}^{-2}\text{s}^{-1}$ .

We are currently investigating two options to read out the signals from the wires. The first option would be to use the same preamplifier as the one developed for the CLAS inner calorimeter and improved for the Heavy Photon Search [60] experiment installed in Hall B.

---

<sup>2</sup>This running condition is specific to the proposal “Partonic Structure of Light Nuclei” in the ALERT run group.

<sup>3</sup>The CLAS *eg6* run period was using the RTPC in the same fashion.



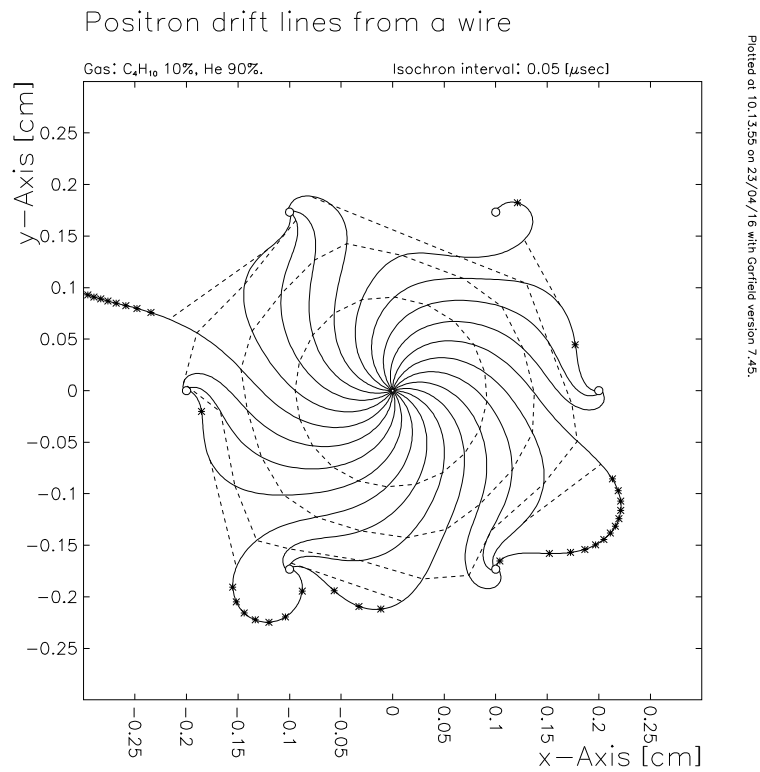


Figure 2.3: Drift lines simulated using MAGBOLTZ [59] for one sense wire (at the center) surrounded by 6 field wires. The two electric field lines leaving the cell disappear when adjusting the voltages on the wires. Dashed lines are isochrones spaced by 50 ns. This shows that the maximum drift time is about 250 ns.

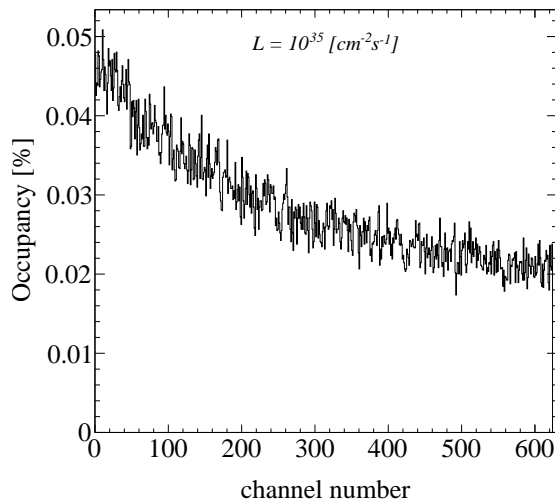


Figure 2.4: A full Geant4 simulation of the ALERT drift chamber hit occupancy at a luminosity of  $10^{35} \text{ cm}^{-2}\text{s}^{-1}$ . The channel numbering starts with the inner most wires and works outwards.

Depending on the gain in the drift chamber and the number of primary ionizations, it is possible to tune the gain of the preamplifier to adapt it to the needs of this experiment. More studies will be needed to evaluate how the gains of the chamber and the preamplifier can be tuned to ensure a noise that allows to select a threshold high enough to be blind to minimum ionizing particles. The time resolution of HPS has been shown to be few-hundred picoseconds for all crystals (Fig. 2.6) which is much better than our requirements.

The second option would be to use the electronics used by the Micromegas of CLAS12, known as the DREAM chip. Its dynamic range and time resolution seem to correspond to the need of our drift chamber. To ensure that it is the case, tests with a prototype will be performed (see section 2.4).

### 2.2.2 The scintillator array

The scintillator array will serve two main purposes. First, it will provide a useful complementary trigger signal because of its very fast response time, which will reduce the random background triggers. Second, it will provide particle identification, primarily through a time-of-flight measurement, but also by a measurement of the particle total energy deposited and path length in the scintillator which is important for doubly charged ions.

The length of the scintillators cannot exceed roughly 40 cm to keep the time resolution below 150 ps. It must also be segmented to match with tracks reconstructed in the drift chamber. Since  ${}^3\text{He}$  and  ${}^4\text{He}$  will travel at most a few mm in the scintillator for the highest anticipated momenta ( $\sim 400 \text{ MeV}/c$ ), a layered scintillator design provides an extra

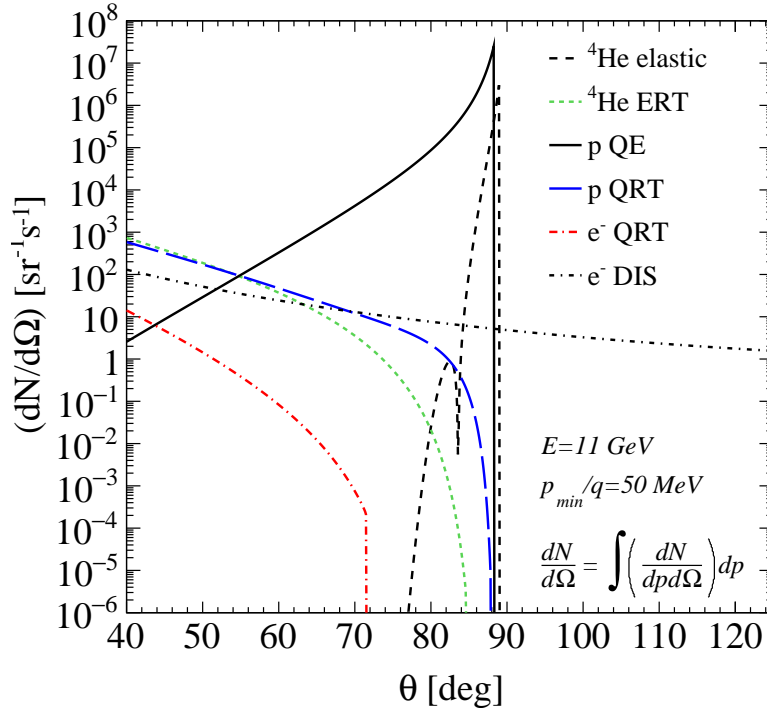


Figure 2.5: The rates for different processes as function of angle. The quasi-elastic radiative tails (QRT),  ${}^4\text{He}$  elastic radiative tail (ERT), and DIS contributions have been integrated over momenta starting at  $p/q = 50 \text{ MeV}/c$ , where  $q$  is the electric charge of the particle detected.

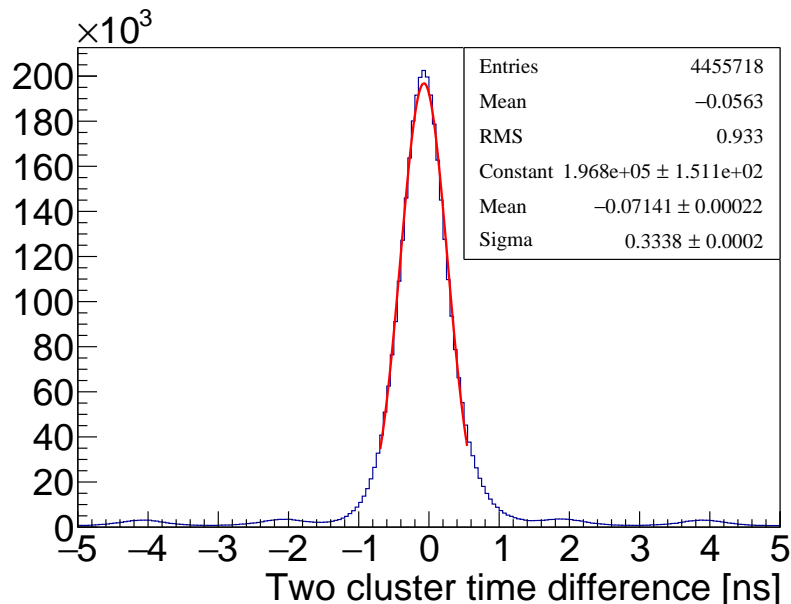


Figure 2.6: Typical time resolution of a crystal for HPS calorimeter.

handle on particle identification by checking if the range exceeded the thickness of the first scintillator layer.

The initial scintillator design consists of a thin (2 mm) inner layer of 60 bars, 30 cm in length, and 600 segmented outer scintillators (10 segments 3 cm long for each inner bar) wrapped around the drift chamber. Each of these thin inner bars has SiPM detectors attached to both ends. A thicker outer layer (18 mm) will be further segmented along the beam axis to provide position information and maintain good time resolution.

For the outer layer, a dual ended bar design and a tile design with embedded wavelength shifting fiber readouts similar to the forward tagger's hodoscope for CLAS12 [61] were considered. After simulating these designs, it was found that the time resolution was insufficient except only for the smallest of tile designs ( $15 \times 15 \times 7$  mm<sup>3</sup>). Instead of using fibers, a SiPM will be mounted directly on the outer layer of a keystone shaped scintillator that is 30 mm in length and 18 mm thick. This design can be seen in Fig. 2.7 which shows a full Geant4 simulation of the drift chamber and scintillators. By directly mounting the SiPMs to the scintillator we collect the maximum signal in the shortest amount of time. With the large number of photons we expect, the time resolution of SiPMs will be a few tens of ps, which is well within our target.

The advantage of a dual ended readout is that the time sum is proportional to the TOF

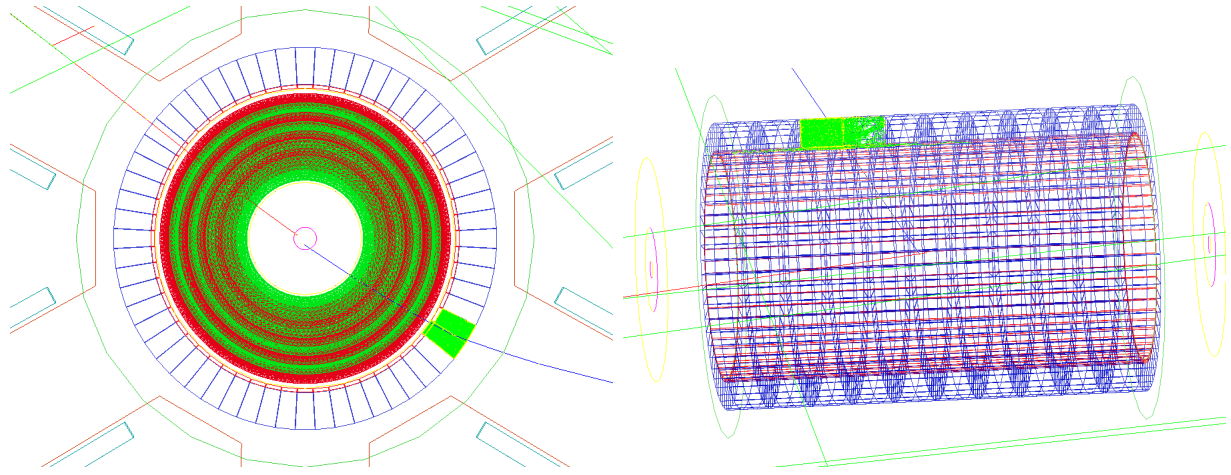


Figure 2.7: Geant4 simulation of a proton passing through the recoil drift chamber and scintillator hodoscope. The view looking downstream (left) shows the drift chamber’s eight alternating layers of wires (green and red) surrounded by the two layers of scintillator (red and blue). Simulating a proton through the detector, photons (green) are produced in a few scintillators.

plus a constant. The improved separation of different particles can be seen in Fig. 2.8. Reconstructing the position of a hit along the length of a bar in the first layer is important for the doubly charged ions because they will not penetrate deep enough to reach the second layer of segmented scintillator.

## 2.3 Reconstruction

The general detection and reconstruction scheme for ALERT is as follows. Fitting a track with the drift chamber and scintillator position information yields a track radius which is proportional to the transverse momentum over the charge. Next, using the scintillator time-of-flight, the particles are separated and identified by their mass-to-charge ratio, therefore leaving a degeneracy for the deuteron and  $\alpha$  particles.

The degeneracy between deuteron and  $\alpha$  particles can be resolved in a few ways. The first and most simple way is to observe that an  $\alpha$  will almost never make it to the second layer and therefore the absence (presence) of a signal would indicate the particle is an  $\alpha$  (deuteron). Furthermore, as will be discussed below, the measured  $dE/dx$  will differ for  ${}^4\text{He}$  and  ${}^2\text{H}$ , therefore, taking into account energy loss in track fitting alone can provide separation. Additionally taking further advantage of the measured energy deposited in the scintillators can help separate the  $\alpha$ s and deuterons.

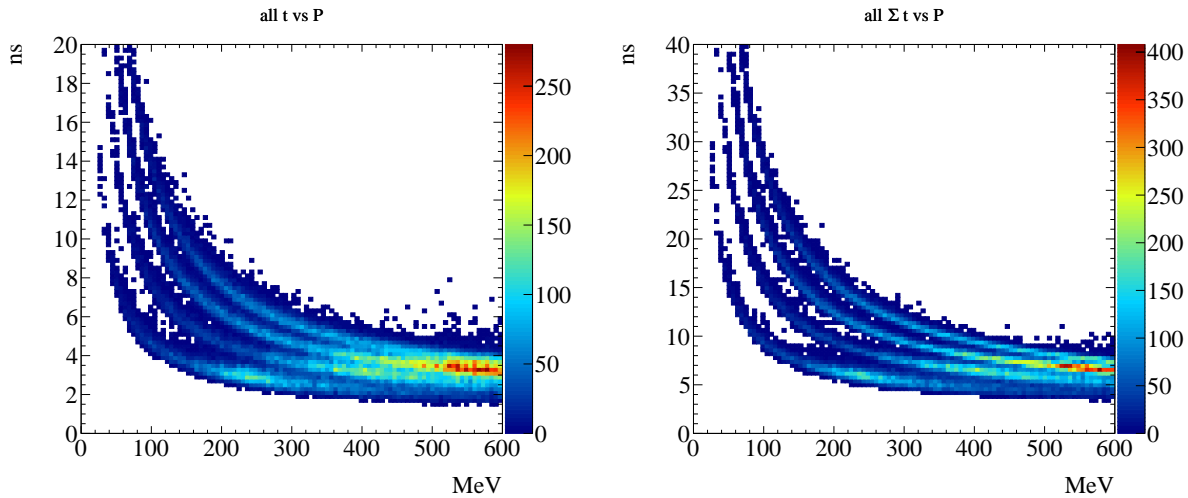


Figure 2.8: Simulated TOF for the various recoil particles vs Momentum. The TOF from just a single readout is shown on the left and the sum of the dual ended readout is shown on the right.

In the studies we present here, we do not include these latter step. However, it is important to point out that extra information is available to us in form of energy deposited in both the drift chamber and the two scintillator layers. In a full (offline) reconstruction these will give extra constraints on the identification but also on the total momentum of the detected nucleus.

As mentioned earlier, we also want a DAQ trigger, that is independent of the CLAS12 triggers. This trigger will be given by the scintillator, in coincidence with signal in a number of layers in the drift chamber. The exact number of drift chamber layers needed for the trigger will be determined during the commissioning based on actual noise and occupancy levels.

### 2.3.1 Track Fitting

The track obtained from a helix fitter is used to determine the coordinates of the vertex and the transverse momentum of the particle. The energy deposited in the scintillators can also be used to determine the kinetic energy of the nucleus. The feasibility and precision of the proposed vertex reconstruction and particle identification scheme were investigated with GEANT4 simulation.

The simulation of the recoil detector has been implemented with the full geometry and

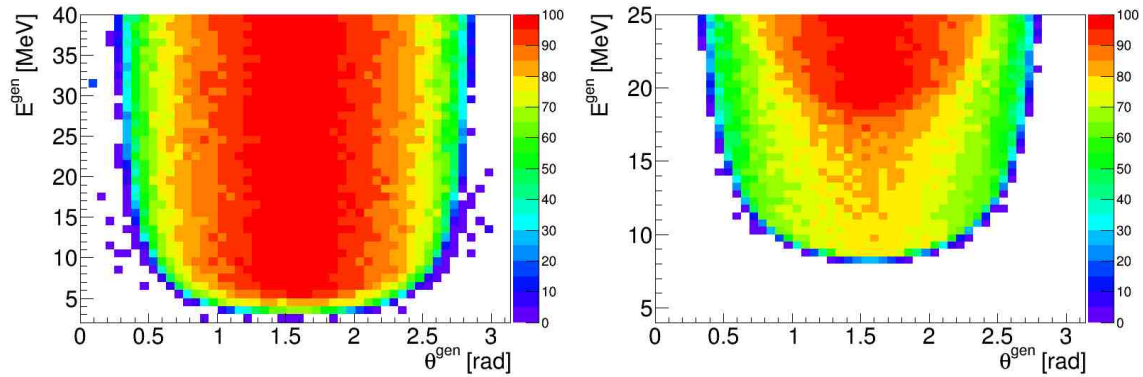


Figure 2.9: Simulated recoil detector acceptance percentage, for protons (left) and  ${}^4\text{He}$  (right), when requiring energy deposition in the scintillators arrays.

material specifications. It includes a 5 Tesla homogeneous solenoid field. The entire detector is filled with a very light gas mixture of He(90%) and  $\text{C}_4\text{H}_{10}$ (10%) set at atmospheric pressure to reduce the energy loss and limit the energy deposition by minimum ionizing particles.

### 2.3.2 Track Reconstruction and Particle Identification

In the current study all recoil species are generated with the same distributions: flat in momentum from threshold up to 40 MeV ( $\sim 250$  MeV/c) for protons and about 25 MeV for other particles; isotropic angular coverage; flat distribution in  $z$ -vertex; and a radial vertex coordinate smeared around the beam line center by a Gaussian distribution of sigma equal to the expected beam radius (0.200 mm).

With the requirement that the particle reaches the scintillator and with a 30 cm length limit, there is a smoothly varying acceptance when averaged over the  $z$ -vertex position. This is shown from simulation in Fig. 2.9 for the lightest and heaviest recoil nuclei. However, this is a conservative estimate, since it only uses tracking information. A more elaborate PID scheme may be able to accommodate a larger acceptance for lower energy recoils.

First, the tracking capabilities of the recoil detector are investigated assuming a spatial resolutions of  $200 \mu\text{m}$  for the drift chamber. The wires are strung in the  $z$ -direction with a stereo angle of  $10^\circ$ . For particles stopped in the scintillators, the resulting difference between generated and reconstructed variables from simulation is shown in Fig. 2.10 for  ${}^4\text{He}$  particles. The momentum for protons and  ${}^4\text{He}$  was also reconstructed (Fig. 2.11) from the radius of the helix assuming a uniform 5 T field. From these plots, it is clear that the resolutions required are fulfilled.

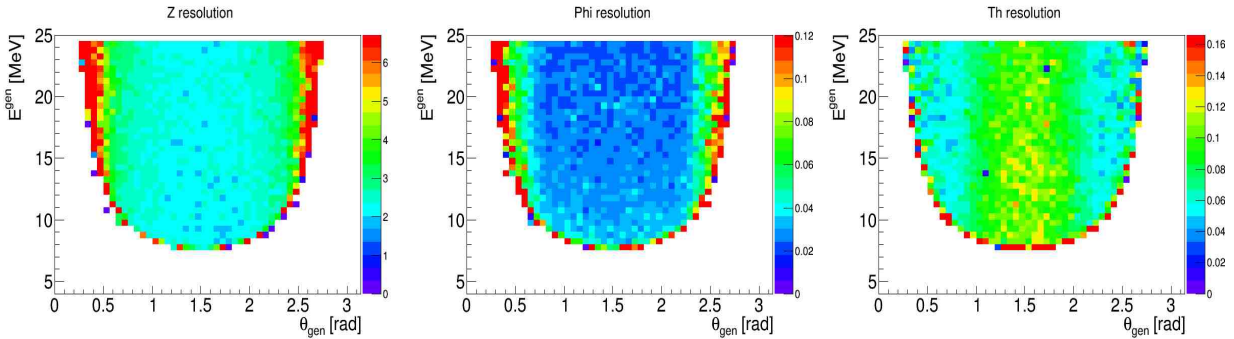


Figure 2.10: Simulated resolutions, integrated over  $z$  for  ${}^4\text{He}$ , of the  $z$ -vertex (in mm) and the polar and azimuthal angles (in rad) for the lowest energy regime when the recoil track reaches the scintillator. Note the  $z$ -axis is in units of percent.

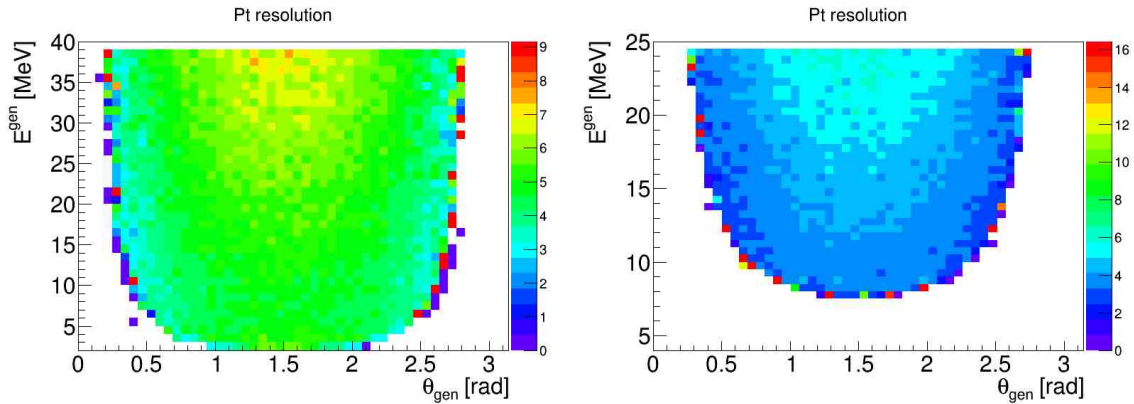


Figure 2.11: Simulated momentum resolutions for proton (left) and  ${}^4\text{He}$  (right) integrated over  $z$ , when the recoil track reaches the scintillators array. Note the  $z$ -axis is in units of percent.



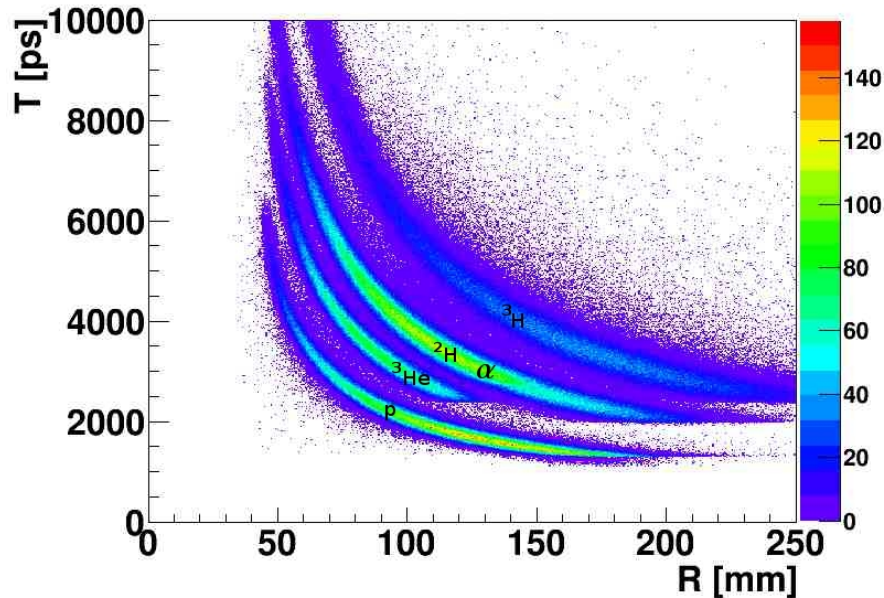


Figure 2.12: Simulated time of flight at the scintillator versus the reconstructed radius in the drift chamber. The bottom band corresponds to proton, next band is the  ${}^3\text{He}$  nuclei,  ${}^2\text{H}$  and  $\alpha$  are overlapping in the third band, the uppermost band is  ${}^3\text{H}$ .  ${}^2\text{H}$  and  $\alpha$  are separated using  $dE/dx$ .

Next, the particle identification scheme is investigated. The scintillators have been designed to ensure a 150 ps time resolution. To determine the  $dE/dx$  resolution, measurements will be necessary for the scintillators and for the drift chamber as this depends on the detector layout, gas mixture, its electronics, voltages... Nevertheless, from [62], one can assume that with the 8 drift chamber measurements and the measurements in the scintillators, the energy resolution should be around 10% or better.

Under those conditions, a clean separation of three of the five nuclei is shown in Fig. 2.12 which represents the time of arrival in the scintillator as a function of the reconstructed radius in the drift chamber.  ${}^2\text{H}$  and  $\alpha$  are separated using  $dE/dx$  in the drift chamber and in the scintillators.

To quantify the separation power of our device, we simulated an equal quantity of each species. We obtained a particle identification efficiency of 99% for protons, 95% for  ${}^3\text{He}$  and 98% for  ${}^3\text{H}$  and around 90% for  ${}^2\text{H}$  and  $\alpha$  with equally excellent rejection factors. It is important to note that for this analysis, only the energy deposited in the scintillators was used, not the energy deposited in the drift chamber nor the path length in the scintillators, thus

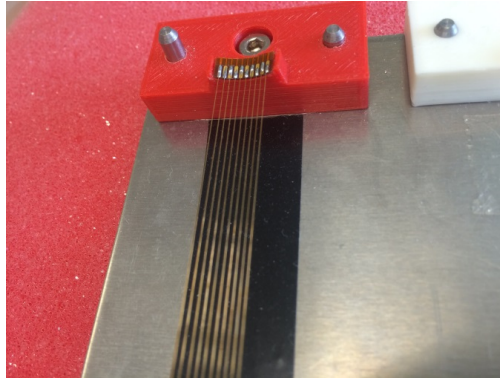


Figure 2.13: Welded wires on a curved structure with a 2 mm gap between each wire.

these number are very conservative. This analysis suggests that the proposed reconstruction and particle identification schemes for this design are quite promising. Studies, using both software and prototyping, are ongoing to determine the optimal detector parameters to minimize the detection threshold while maximizing particle identification efficiency. The resolutions presented above have been implemented in a fast Monte-Carlo used in the next section to evaluate the impact on our measurements.

## 2.4 Drift chamber prototype

Since the design of the drift chamber presents several challenges, we decided early to start the R&D for the project and build a prototype to investigate the feasibility. This section presents the work done in Orsay to address the main questions concerning the mechanics that needed to be answered:

- Can we build a stereo drift chamber with a 2 mm gap between wires?
- Can we design a frame that can be quickly changed in case of a broken wire?
- Can the forward structure be both light to reduce the multiple scattering and rigid enough to support the tension due to the wires?

For the first question, small plastic structures realized with a 3D printer were tested and wires welded on it, as shown in Fig. 2.13. This demonstrated our ability to weld wires with a 2 mm gap on a curved structure.

To limit issues related to broken wires, we opted for a modular detector made of identical sectors. Each sector covers  $20^\circ$  of the azimuthal angle (Fig. 2.14) and can be rotated around the beam axis to be separated from the other sectors. This rotation is possible due to the absence of one sector, leaving a  $20^\circ$  dead angle. Then, if a wire breaks, its sector can be

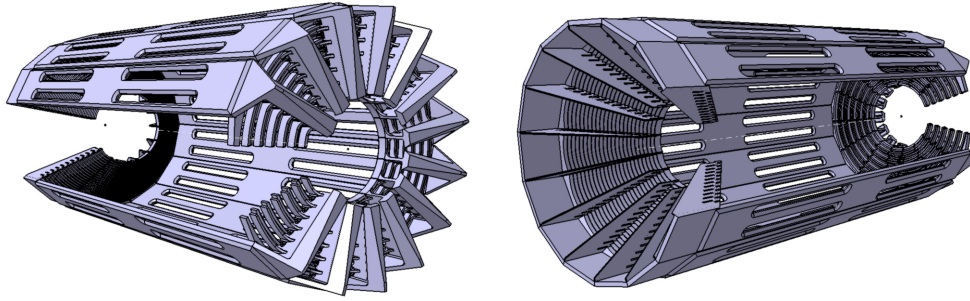


Figure 2.14: Upstream (left) and downstream (right) ends of the prototype detector in CAD with all the sectors included.

removed independently and replaced by a spare. Plastic and metallic prototype sectors were made with 3D printers to test the assembling procedure and we have started the construction of a full size prototype of one sector.

The shape of each sector is constrained by the position of the wires. It has a triangular shape on one side and due to the stereo angle, the other side looks like a pine tree with branches alternatively going left and right from a central trunk (Fig. 2.15).

The last question about the material used to build the structure will be studied in details with future prototypes. Nevertheless, current design plans are to use carbon in place of the aluminum in the forward region and titanium for the backward structure. The prototype was designed to check the mechanical requirements summarized above but also to verify the different cell configurations, and to test the DREAM electronics (time resolution, active range, noise). Since a total of five sectors have been build for tests, this will allow us to check that the elements can be properly positioned relatively to each other and one sector will be completely equipped with wires to be tested with a cosmic test bench and an  $\alpha$  source.

## 2.5 Other options for a Low Energy Recoil Detector

We explored other available solutions for the low-energy recoil tracker (ALERT) with adequate momentum and spatial resolution, and good particle identification for recoiling light nuclei ( $p$ ,  ${}^3\text{H}$  and  ${}^3\text{He}$ ). After investigating the feasibility of the proposed measurements using the CLAS12 Central Detector and the BoNuS Detector [50, 44], we concluded that we needed to build a dedicated detector. We summarize in the following the facts that led us to this conclusion.

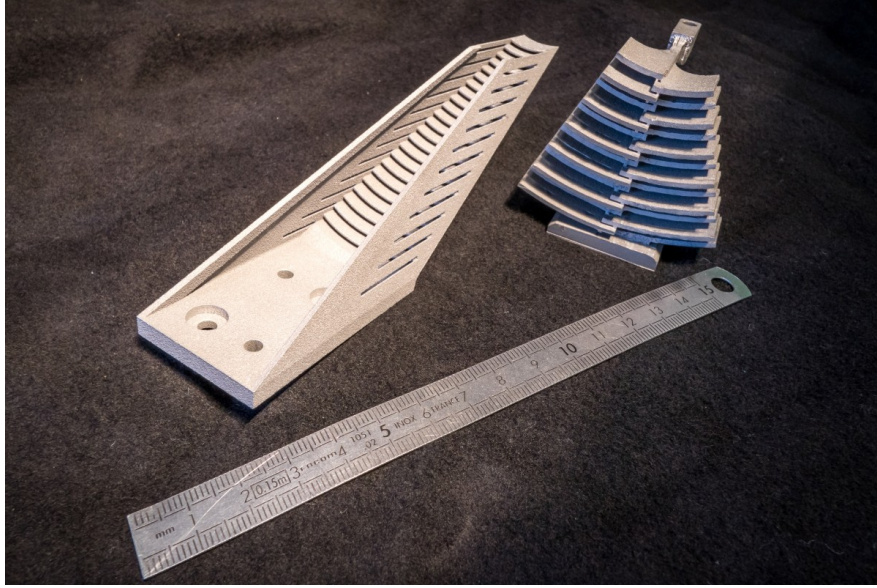


Figure 2.15: Mechanics of one sector for the prototype made with 3D printer.

### 2.5.1 Central Detector

The CLAS12 Central Detector [55] is designed to detect various charged particles over a wide momentum and angular range. The main detector package includes:

- Solenoid Magnet: provides a central longitudinal magnetic field up to 5 Tesla, serves to curl emitted low energy Møller electrons and determine particle momenta through tracking.
- Central Tracker: consists of 3 layers of silicon strips and 3 layers of Micromegas. The thickness of a single silicon layer is  $300\mu\text{m}$ .
- Central Time-of-Flight: an array of scintillator paddles with a cylindrical geometry of radius 26 cm and length 50 cm; the thickness of the detector is 2 cm with designed timing resolution of  $\sigma_t = 50$  ps, used to separate pions and protons up to 1.2 GeV/ $c$ .

The current design, however, is not optimal for low energy particles ( $p < 300$  MeV/ $c$ ) due to the energy loss in the first 2 silicon strip layers. The momentum detection threshold is  $\sim 200$  MeV/ $c$  for protons,  $\sim 350$  MeV/ $c$  for deuterons and even higher for  $^3\text{H}$  and  $^3\text{He}$ . These values are significantly too large for our proposed measurements, which makes the CLAS12 central detector not suitable for our measurements.

Detectors	RTPC	New Tracker
Drift region radius	4 cm	5 cm
Longitudinal length	$\sim 40$ cm	$\sim 40$ cm
Gas mixture	80% helium/20% DME	90% helium/10% isobutane
Azimuthal coverage	$360^\circ$	$340^\circ$
Momentum range	70-250 MeV/ $c$ protons	70-250 MeV/ $c$ protons
Transverse mom. resolution	10% for 100 MeV/ $c$ protons	10% for 100 MeV/ $c$ protons
$z$ resolution	3 mm	3 mm
Solenoidal field	$\sim 5$ T	$\sim 5$ T
ID all light nuclei	No	Yes
Trigger	can not be included	can be included

Table 2.2: Comparison between the RTPC (left column) and the new tracker (right column).

### 2.5.2 BoNuS12 Radial Time Projection Chamber

The original BoNuS detector was built for Hall B experiment E03-012 to study neutron structure at high  $x_B$  by scattering electrons off an almost on-shell neutron inside deuteron. The purpose of the detector was to tag the low energy recoil protons ( $p > 60$  MeV/ $c$ ). The key component for detecting the slow protons was the Radial Time Projection Chamber (RTPC) based on Gas Electron Multipliers (GEM). A later run period (eg6) used a  $^4\text{He}$  gas target and a newly built and improved RTPC to detect recoiling  $\alpha$  particles in coherent DVCS scattering. The major improvements of the eg6 RTPC were full cylindrical coverage and a higher data taking rate.

The approved 12 GeV BoNuS (BoNuS12) proposal is planning to use a similar device with some upgrades. The target gas cell length will be doubled, and the new RTPC will be longer as well, leading to a doubling in luminosity and an increased acceptance. Taking advantage of the larger bore ( $\sim 700$  mm) of the 5 Tesla solenoid magnet, the maximum radial drift length will be increased from the present 3 cm to 4 cm, improving the momentum resolution by 50% [44] and extending the momentum coverage. The main features of the proposed BoNuS12 detector are summarized in Table 2.2.

In principle, particle identification can be obtained from the RTPC through the energy loss  $dE/dx$  in the detector as a function of the particle momentum (see Fig. 2.16). However, with such a small difference between  $^3\text{H}$  and  $^3\text{He}$ , it is nearly impossible to discriminate between them on an event by event basis because of the intrinsic width of the  $dE/dx$  distributions. This feature is not problematic when using deuterium target, but makes the RTPC no longer a viable option for our tagged EMC and tagged DVCS measurements which require a  $^4\text{He}$  target and the detection of  $^4\text{He}$ ,  $^3\text{He}$ ,  $^3\text{H}$ , deuterons and protons.

Another issue with the RTPC is its slow response time due to the long drift time

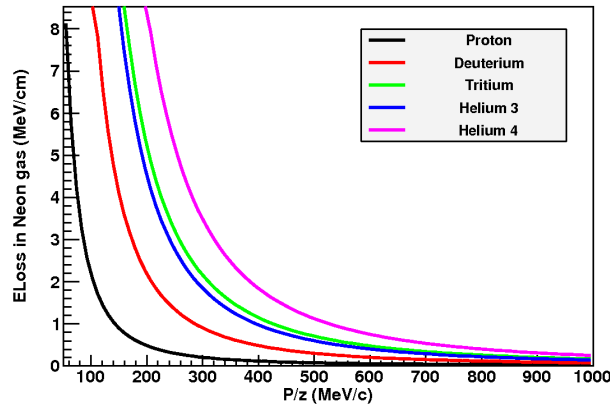


Figure 2.16: Calculation of energy loss in Neon gas as a function of the particle momentum divided by its charge for different nuclei.

( $\sim 5\mu\text{s}$ ). If a fast recoil detector could be included in the trigger it would have a significant impact on the background rejection. Indeed, in about 90% DIS on deuteron or helium the spectator fragments have too low energy or too small angle with the beam line to get out of the target to be detected. Since the data acquisition speed was the main limiting factor for both BoNuS and eg6 runs in CLAS, including the recoil detector in the trigger would allow us to run at higher luminosities. Indeed events without a hit in the recoil detector would not be recorded and this will significantly reduce the trigger's frequency.

### 2.5.3 Summary

As explained in the previous sections, the threshold of the CLAS12 inner tracker is clearly too high to be used for our measurements. On the other hand, the recoil detector planned for BoNuS12, a RTPC, is not suitable due to its inability to distinguish all kind of particles we need to measure. Moreover, as the RTPC cannot be efficiently included in the trigger, a lot of background events are sent to the readout electronics, which will cause its saturation and limit the maximum luminosity the detector can handle. Therefore, we propose to use A Low Energy Recoil Tracker (ALERT) based on a new detector design, described in the previous sections, that would provide good timing and energy loss information and a total energy measurement for each track. The fast timing will allow a tight time coincidence with CLAS12, thereby reducing the background that was encountered in previous RTPC detectors. The recoil detector can be included in the data acquisition trigger, which will significantly reduce triggering on events from the target windows, which are outside the acceptance and events with recoil too slow to exit the target.

Finally, the use of time of flight and  $dE/dx$  measurements will provide improved particle

identification for the recoiling nuclei without ambiguity for  ${}^3\text{H}$  and  ${}^3\text{He}$  identification. The features and requirements for this new detector are compared with the current RTPC design for BoNuS12 in Table 2.2. The transverse momentum and  $z$  resolution are chosen following the BoNuS specifications.

## 2.6 Technical contributions from the research groups

This effort is led by four research groups, Argonne National Lab (ANL), Institut de Physique Nucléaire d'Orsay (IPNO), Jefferson Lab and Temple University (TU).

Jefferson Lab is the host institution. ANL, IPNO and TU have all contributed technically to CLAS12. ANL was involved in the construction of the high-threshold Cherenkov counters (HTCC) for CLAS12. ANL has a memorandum of understanding (MOU) with JLab on taking responsibility for the HTCC light collection system including testing the photomultipliers and the magnetic shielding. For the RICH detector for CLAS12, ANL developed full GEANT-4 simulations in addition to the tracking software. ANL also developed the mechanical design of the detector support elements and entrance and exit windows in addition to the front-end electronics cooling system. IPNO took full responsibility for the design and construction of CLAS12 neutron detector (CND). The CND was successfully delivered to Jefferson Lab. TU played an important role in the refurbishment of the low threshold Cherenkov counters (LTCC), which was completed recently. All 216 photomultipliers have been coated with wavelength shifting material (p-Terphenyl) at Temple University, which resulted in a significant increase in the number of photoelectrons response.

The three institutions have already shown strong technical commitment to JLab 12 GeV upgrade, with a focus on CLAS12 and this proposal is a continuation of that commitment.

### 2.6.1 Argonne National Laboratory and Temple University

The ANL medium energy group is responsible for the ALERT scintillator system, including scintillation material, light collection device and electronics. First results of simulations have led to the design proposed here. This work will continue to integrate the scintillator system with the wire chamber. ANL will collaborate closely with Temple University to test the light detection system. Both institutions will be responsible to assemble and test the detector.

### 2.6.2 Institut de Physique Nucléaire d'Orsay

The Institut de Physique Nucléaire d'Orsay is responsible for the wire chamber and the mechanical structure of the detector design and construction. As shown in the proposal, this work has already started as part of a wider R&D program focused on nuclear fragments

detection with light wire chambers. A first prototype is being built to test different cell forms, wire material, wire thickness, pressure, etc. This experience will lead to a complete design of the ALERT detector integrating the scintillator built at ANL, the gas distribution system and the electronic connections. The funding already secured for this program should allow for the construction of these mechanical parts and the wire chamber itself.

Funding is also available, in partnership with *CEA Saclay*, to test the use of the DREAM front-end chip for our wire chamber. Further tests are planned to adapt the electronics to the ALERT chamber or test other chips. This chip will be used for the CLAS Micromegas, so we expect its integration to be straightforward when the ALERT run group will need it.

### 2.6.3 Jefferson Laboratory

We expect Jefferson Laboratory to help with the settings of the beam line. In particular, the maximum beam current will be around 500 nA for the run at  $10^{35} \text{ cm}^{-2}\text{s}^{-1}$ , which is not common for Hall-B. We also expect JLab to design and build the target for the experiment as it will be a very similar target as the ones build for CLAS Bonus and eg6 run.

We also expect Jefferson Laboratory to provide assistance in the detector installation in the Hall and to connect the electronics of ALERT to the acquisition and trigger systems of CLAS12 in addition to slow controls.



# Chapter 3

## Proposed Measurements

In light of the physics motivation presented and the capabilities of the new ALERT detector, we propose to measure the tagged deep-inelastic scattering off  $^2\text{H}$  and  $^4\text{He}$  and for a range of the recoiling spectator momenta  $P_{A-1}$  from 70 to 400 MeV/ $c$ . We choose the helium target for several reasons, first it is a light gas that can easily be used in a very light gaseous target allowing to detect very low momentum spectators. Also, calculation for FSI are theoretically very challenging, keeping the number of nucleon low is therefore of great help; moreover, as spectators get heavier, their detection threshold increases, which explains why we want to use low  $A$  target. The reactions we are going to study are:

- $^2\text{H}(e, e'p)X$  — bound neutron;
- $^4\text{He}(e, e' ^3\text{H})X$  — bound proton;
- $^4\text{He}(e, e' ^3\text{He})X$  — bound neutron;

### 3.0.4 Monte-Carlo Simulation

To estimate the rates of our experiment and provide meaningful estimates of our statistical error bars, we developed a Monte-Carlo simulation based on PYTHIA with some basic nuclear effects. The interaction on the nucleon is generated in a basic impulse approximation, neglecting the off-shellness of the target nucleon. We simulate the Fermi motion of the nucleons in the target nuclei according to the distribution provided by AV18+UIX potentials [63, 64, 65]. This leads to a target nucleon with momentum  $\vec{p}_n$  and the nuclear spectator is generated with a kinematic opposite to the interacting nucleon,  $-\vec{p}_n$ . The PYTHIA Monte-Carlo provides simulation for the DIS interaction and the fragmentation of the partons, we do not include nuclear effects such as FSI here.

In the simulation, we select DIS by requesting  $Q^2 > 1.5 \text{ GeV}^2$  and  $W > 2 \text{ GeV}$ . These are the same for all figures, indication on the figures are for the theoretical predictions. In

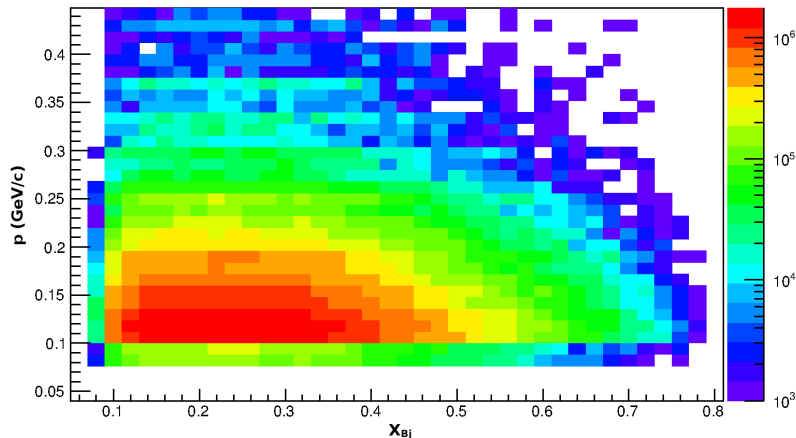


Figure 3.1: Expected event count as a function of  $x_B$  and the recoil momentum of the  ${}^3\text{H}$  from a  ${}^4\text{He}$  target.

our experimental configuration and with the cut described above, we expect  $\langle Q^2 \rangle \sim 3 \text{ GeV}^2$ .

The generated final-state particles undergo acceptance tests. Electrons, which will be detected by the forward detector, are treated by a GEANT4 Monte-Carlo simulation of CLAS12. The recoiling nuclei (including protons) acceptance is based on the GEANT4 simulation described in section 2.3 and represented in Fig. 2.9. On top of these estimates, we apply an overall 75% efficiency to this detection settings to account for the fiducial cuts and detector inefficiencies.

### 3.0.5 Beam Time Request

We estimate, based on past measurements with CLAS, that the ratios we want to measure will be affected by systematic errors of  $\sim 3$  percents. Our beam time request, allows to have the statistical error bars of our key measurement (Fig. 3.4 right) comparable to the systematic ones. Assuming the luminosity of  $3 \cdot 10^{34} \text{ cm}^{-2}\text{s}^{-1}$ , the beam time request for proposed measurements is of 20 days for each target.

## 3.1 Projections

Based on our simulation, we determine the available kinematic range and production rates accessible for each channel. The  $x_B$  and recoil momenta distributions are illustrated in Fig. 3.1 for tagged  ${}^3\text{H}$  out of an  ${}^4\text{He}$  target. This figure shows the available phase space for a measurement of the bound proton structure function.

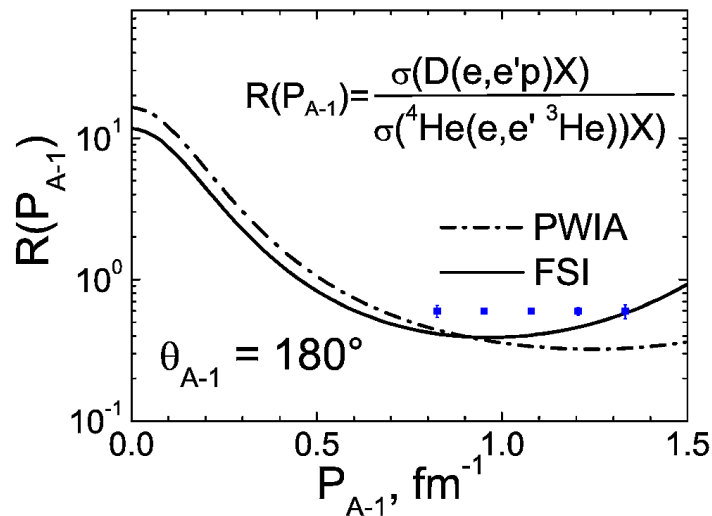


Figure 3.2: This figure is similar to Fig. 1.2, it shows the predictions for CLAS12 kinematic [24, 66] of the ratio  $R(^4\text{He}, ^2\text{H}, |\vec{P}_{A-1}|)$  compared to projected statistical error bars for the proposed experiment (blue points).

### 3.1.1 Testing the Spectator Model

The projections presented in Fig. 3.2 show the capability of this experiment to measure cross section ratios of DIS on a bound nucleon in light nuclei and, therefore, our capability to check the validity of the spectator model used by the theoretical predictions. Statistical error bars in this figure are very modest and even smaller than the points on the logarithmic scale. It is therefore clear that we have capability to test the spectator model in detail.

The high precision we can obtain for this channel should lead to more valuable confirmation of assumptions made for other similar measurements, such as BoNuS. We will be able to carry out, multi-dimensional test for the FSI models as was done in [67] and for the first time perform similar studies on helium. Other tests have been proposed to insure that outgoing pions are formed far enough from the nuclei to limit FSI [68, 69] and understand the color transparency effect associated. This study is most sensitive to spectators emitted at  $90^\circ$ , where the effect is larger, and can then be extrapolated to lower angles. In Ref. [52], testing that the  $x_B$  scaling holds in tagged DIS is proposed as another way to confirm the soundness of the method.

Due to its high statistics, the experiment will therefore have the possibility to make thorough test of the spectator mechanism and its limits. In particular it will, for the first time, experimentally explore this framework for  $A > 2$ , opening completely new opportunities for light nuclei tagged experiments.

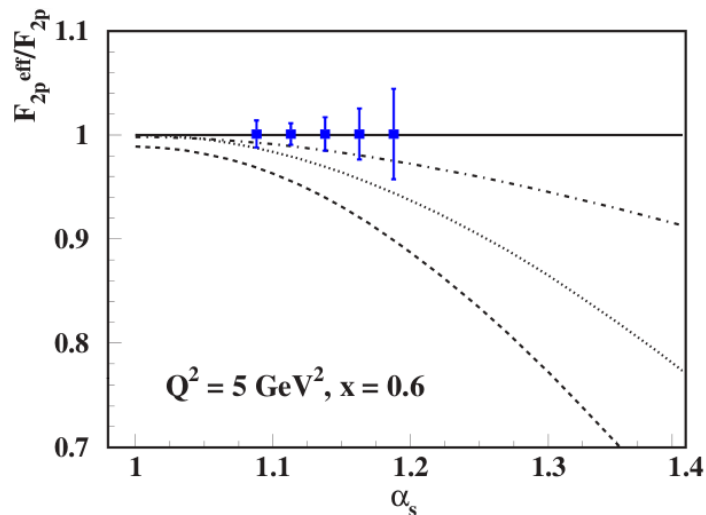


Figure 3.3: This figure is similar to Fig. 1.3, it shows the predictions from [40] of the ratio  $F_{2p}^{bound}/F_{2p}$  compared to projected statistical error bars for the proposed experiment (blue points).

### 3.1.2 EMC effect in deuterium

As explained in the first chapter, it is possible to enhance the EMC effect in the deuteron by selecting the highly off-shell nucleons. This prediction can be directly tested with our proposed experiment, as shown in Fig. 3.3 where we compare our measurement capabilities to Melnitchouk *et al.* [40] predictions using several models. Note that in our case, the proton being tagged, we are actually measuring  $F_{2n}^{bound}/F_{2n}$ , but this measurement can be interpreted similarly to the proton case in regard to the EMC effect. The main limitation in this channel is the very fast decrease of the cross section for high  $\alpha$  in deuterium.

We point out that such a measurement is also possible with the helium target, for either the proton or the neutron. This would allow to reach much higher *alpha* without running a prohibitively long experiment. We do not present these projections here because there is no theoretical predictions for these channels. The main reason is the difficulty to extend the calculations to the helium four-body system. However, we hope that the approval of the proposal can trigger further study in this regard and that predictions will be available by the time our proposed experiment is ready to run.

### 3.1.3 Testing the Rescaling Models

The main goal of our experiment is to discriminate decisively between models of EMC, Fig. 3.4 illustrates this capability. We have here a high differentiation power between  $x$ -rescaling and  $Q^2$ -rescaling models. We note the good coverage and small

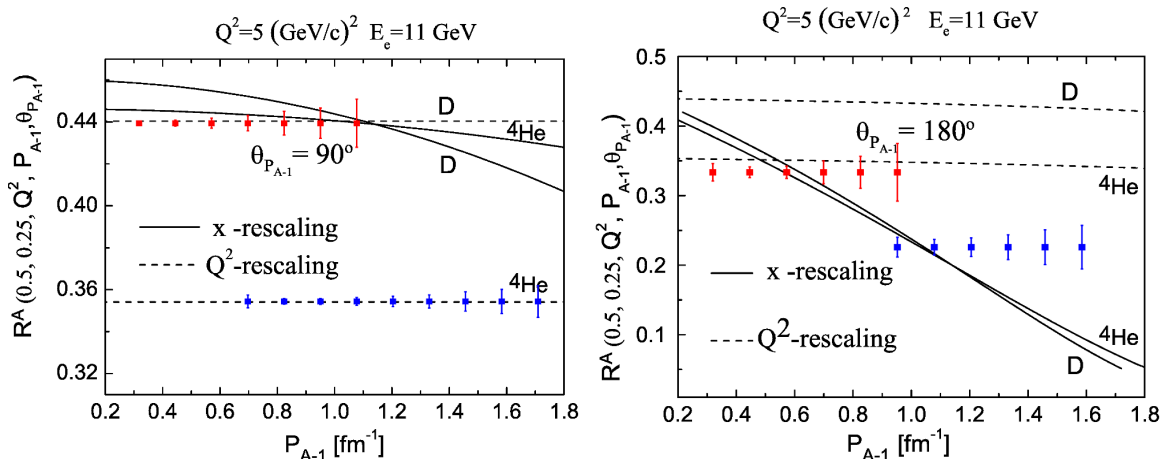


Figure 3.4: This figure is similar to figure 1.4, it shows predictions of the ratio  $R^A(x, x')$  for  $A = 2$  and  $A = 4$  as a function of the momentum of the recoil nucleus  $A - 1$  at perpendicular (left) and backward (right) angle. The full and dashed curves are predictions for CLAS12 kinematic [24, 66] of the  $x$ -rescaling (binding) and  $Q^2$ -rescaling models, respectively, points are projections for  ${}^2\text{H}$  (red) and  ${}^4\text{He}$  (blue).

error bars for  $\theta_{P_{A-1}} = 90^\circ$  ( $75 < \theta_{P_{A-1}} < 105^\circ$ ). This is due to the better acceptance for this angle. The measurement at backward angle ( $\theta_{P_{A-1}} > 150^\circ$ ), however, is much more difficult and is the main constraint driving our beam time request. Still, in order to obtain our planned precision with a reasonable beam time request, the backward angles are selected from  $150^\circ$  and up instead of the  $160^\circ$  which is used for the theory predictions.

We notice the complementarity of our choice of targets in the phase space covered, this is due to the fact that larger recoil nuclei are more absorbed by the target material and have higher detection threshold. At the same time, the Fermi momentum is larger in helium allowing better statistics at high  $p_{A-1}$ . Using helium is then also an opportunity to explore higher spectator momentum with a reasonable beam time request.

### 3.1.4 Tagged EMC Ratio

The experiment can also confront the striking predictions for backward versus forward tagged EMC in binding models, as illustrated in the Fig. 3.5. We see that the model prediction will be clearly tested, however the reach in  $x_B$  for the backward recoils is also strongly constrain by the beam time available for the experiment. Indeed, the strongest effect is expected at  $x_B \sim 0.5$  for which we need high statistics.

The measurement of the tagged EMC ratio is a very clean observable even for other kinds of model, in the low momentum regime one should be able to reproduce very nicely

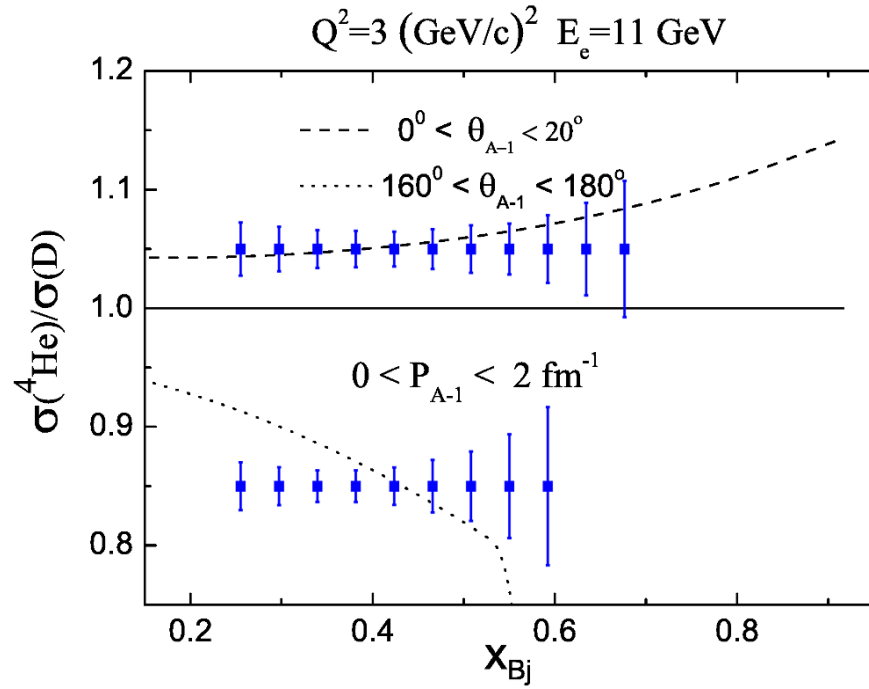


Figure 3.5: This figure is similar to figure 1.5, it shows the semi-inclusive EMC ratio  $R_0(x, Q^2)$  as a function of  $x_B$  with recoils emitted forward and backward, the dashed and dotted curves are predictions for the local EMC effect for CLAS12 kinematic [24, 66] the blue points are statistical error bar projections for our measurement.

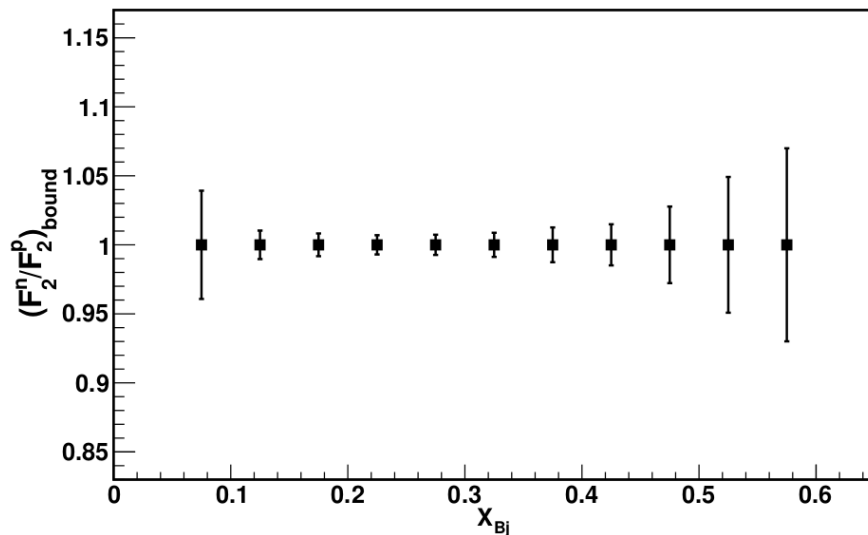


Figure 3.6: Statistical error bar projections for the ratio  $F_2^n/F_2^p$  for bound nucleons as a function of  $x_{Bj}$  using an  ${}^4\text{He}$  target.

the classic EMC effect and then be able to study its dependence to the spectator angle and momentum. As was shown before, the different models offer very different predictions, in particular, models based only on off-shellness give a ratio of 1 when we select the same spectator kinematic.

### 3.1.5 The Flavor Dependent Nuclear Effects

Finally with our experimental setup, we will explore the flavor dependence of nuclear PDFs. Figure 3.6 illustrates our capabilities, for  ${}^4\text{He}$  the isovector model predicts a ratio of 1 [54], but others predict that nuclear effects change the d/u ratio and should therefore be observed here [53]. We will be able to explore any variation in bound nucleons with 1 to 2% statistical error bars – *i.e.* 4% when including expected systematic error bars – from  $x_B$  of 0.1 to 0.5.

# Summary and Beam Time Request

In summary, we proposed a tagged DIS measurement on light nuclear targets ( $^2\text{H}$  and  $^4\text{He}$ ) by detecting the backward recoiling spectators. By taking the advantage of the high luminosity and large kinematic coverage of CLAS12, we will be able to cover a wide range in spectator kinematic insuring a good control over FSI effects.

In order to make this measurement, we propose to use a new recoil detector to fit our experimental needs in term of low energy nuclei detection. The detector is designed such that it will provide good timing resolution and particle identification. Prototyping of this detector is currently underway in Orsay as part of a larger R&D program on drift chambers.

We propose to measure various tagged ratios and double ratios with their dependencies on the recoil kinematics. These measurements will provide very stringent tests of numerous models for the EMC and anti-shadowing effects and, more importantly, a model independent insight into the origin of the EMC effect in term of  $x_B$  or  $Q^2$ -rescaling.

In order to achieve all the goals presented in this proposal, we need 45 days of running. With 11 GeV electron beam at  $3.10^{34} \text{ cm}^{-2}\text{s}^{-1}$  ( $= 150 \text{ nA}$ ) with helium and deuterium targets (20 days each) and 5 days of commissioning of the ALERT detector at 11 GeV and 2.2 GeV (2.5 days each) at various luminosities with helium and hydrogen targets.

## Relation to other proposals

Our proposal has similar and rather complementary goals compared to the approved PR12-11-107 [45] and PR12-11-003A [46] proposals. There are however several important differences. The goal of these proposals is to tag fast neutrons when scattering electrons off a deuteron target. While, the goal of our measurements is to tag protons at slightly smaller energies when scattering electrons off deuteron and tag  $^3\text{H}$  and  $^3\text{He}$  when the target is  $^4\text{He}$ . Together these three measurements will provide a more complete picture of all the tagging options. Therefore we consider them complementary. As the tagging method is still relatively new, it is a good opportunity to fully understand the process and identify the most promising channels for future experiments at JLab 12 GeV and beyond at an electron ion collider.



# Bibliography

- [1] J. J. Aubert *et al.*, “The ratio of the nucleon structure functions  $F_2^n$  for iron and deuterium,” *Phys. Lett.*, vol. B123, pp. 275–278, 1983.
- [2] J. Ashman *et al.*, “Measurement of the Ratios of Deep Inelastic Muon - Nucleus Cross-Sections on Various Nuclei Compared to Deuterium,” *Phys.Lett.*, vol. B202, p. 603, 1988.
- [3] M. Arneodo *et al.*, “Shadowing in Deep Inelastic Muon Scattering from Nuclear Targets,” *Phys.Lett.*, vol. B211, p. 493, 1988.
- [4] M. Arneodo *et al.*, “Measurements of the nucleon structure function in the range  $0.002 - \text{GeV}^2 < x < 0.17 - \text{GeV}^2$  and  $0.2 - \text{GeV}^2 < q^2 < 8 - \text{GeV}^2$  in deuterium, carbon and calcium,” *Nucl.Phys.*, vol. B333, p. 1, 1990.
- [5] J. Gomez *et al.*, “Measurement of the A-dependence of deep inelastic electron scattering,” *Phys.Rev.*, vol. D49, pp. 4348–4372, 1994.
- [6] D. Allasia *et al.*, “Measurement of the neutron and the proton F2 structure function ratio,” *Phys.Lett.*, vol. B249, pp. 366–372, 1990.
- [7] J. Seely *et al.*, “New measurements of the EMC effect in very light nuclei,” *Phys. Rev. Lett.*, vol. 103, p. 202301, 2009.
- [8] D. F. Geesaman, K. Saito, and A. W. Thomas, “The nuclear EMC effect,” *Ann. Rev. Nucl. Part. Sci.*, vol. 45, pp. 337–390, 1995.
- [9] P. R. Norton, “The EMC effect,” *Rept. Prog. Phys.*, vol. 66, pp. 1253–1297, 2003.
- [10] S. Malace, D. Gaskell, D. W. Higinbotham, and I. Cloet, “The Challenge of the EMC Effect: existing data and future directions,” *Int.J.Mod.Phys.*, vol. E23, p. 1430013, 2014.
- [11] M. Ericson and A. W. Thomas, “Pionic Corrections and the EMC Enhancement of the Sea in Iron,” *Phys. Lett.*, vol. B128, p. 112, 1983.
- [12] G. V. Dunne and A. W. Thomas, “DEEP INELASTIC SCATTERING AS A PROBE OF NUCLEON AND NUCLEAR STRUCTURE,” *Nucl. Phys.*, vol. A446, pp. 437c–443c, 1985.

- [13] S. V. Akulinichev, S. A. Kulagin, and G. M. Vagradov, "The Role of Nuclear Binding in Deep Inelastic Lepton Nucleon Scattering," *Phys. Lett.*, vol. B158, pp. 485–488, 1985.
- [14] H. Jung and G. A. Miller, "NUCLEONIC CONTRIBUTION TO LEPTON NUCLEUS DEEP INELASTIC SCATTERING," *Phys. Lett.*, vol. B200, pp. 351–356, 1988.
- [15] F. E. Close, R. G. Roberts, and G. G. Ross, "The Effect of Confinement Size on Nuclear Structure Functions," *Phys. Lett.*, vol. B129, p. 346, 1983.
- [16] O. Nachtmann and H. J. Pirner, "Color Conductivity in Nuclei and the EMC Effect," *Z. Phys.*, vol. C21, p. 277, 1984.
- [17] R. L. Jaffe, F. E. Close, R. G. Roberts, and G. G. Ross, "On the Nuclear Dependence of Electroproduction," *Phys. Lett.*, vol. B134, p. 449, 1984.
- [18] F. E. Close, R. G. Roberts, and G. G. Ross, "Factorization Scale Independence, the Connection between Alternative Explanations of the EMC Effect and QCD Predictions for Nuclear Properties," *Nucl. Phys.*, vol. B296, p. 582, 1988.
- [19] L. Frankfurt and M. Strikman, "POINT - LIKE CONFIGURATIONS IN HADRONS AND NUCLEI AND DEEP INELASTIC REACTIONS WITH LEPTONS: EMC AND EMC LIKE EFFECTS," *Nucl.Phys.*, vol. B250, pp. 143–176, 1985.
- [20] K. Ackerstaff *et al.*, "Nuclear effects on  $R = \sigma(L)/\sigma(T)$  in deep inelastic scattering," *Phys. Lett.*, vol. B475, pp. 386–394, 2000.
- [21] L. Frankfurt and M. Strikman, "High-Energy Phenomena, Short Range Nuclear Structure and QCD," *Phys.Rept.*, vol. 76, pp. 215–347, 1981.
- [22] S. Kumano and F. E. Close, "DEPENDENCE OF THE EMC EFFECT ON NUCLEAR STRUCTURE," *Phys. Rev.*, vol. C41, pp. 1855–1858, 1990.
- [23] C. Ciofi degli Atti and S. Liuti, "Can nuclear binding explain the classical EMC effect?," *Nucl.Phys.*, vol. A532, pp. 241–248, 1991.
- [24] C. Ciofi degli Atti, L. P. Kaptari, and S. Scopetta, "Semi-inclusive deep inelastic lepton scattering off complex nuclei," *Eur. Phys. J.*, vol. A5, pp. 191–207, 1999.
- [25] D. Higinbotham, J. Gomez, and E. Piasetzky, "Nuclear Scaling and the EMC Effect," 2010.
- [26] L. Weinstein *et al.*, "Short Range Correlations and the EMC Effect," *Phys.Rev.Lett.*, vol. 106, p. 052301, 2011.
- [27] L. Frankfurt, M. Strikman, D. Day, and M. Sargsian, "Evidence for short range correlations from high  $Q^{*2}$  (e, e-prime) reactions," *Phys.Rev.*, vol. C48, pp. 2451–2461, 1993.

- [28] K. Egiyan *et al.*, “Observation of nuclear scaling in the  $A(e, e\text{-prime})$  reaction at  $x(B)$  greater than 1,” *Phys.Rev.*, vol. C68, p. 014313, 2003.
- [29] K. Egiyan *et al.*, “Measurement of 2- and 3-nucleon short range correlation probabilities in nuclei,” *Phys.Rev.Lett.*, vol. 96, p. 082501, 2006.
- [30] O. Hen *et al.*, “Momentum sharing in imbalanced Fermi systems,” *Science*, vol. 346, pp. 614–617, 2014.
- [31] C. Ciofi degli Atti *et al.*, “On the dependence of the wave function of a bound nucleon on its momentum and the EMC effect,” *Phys. Rev.*, vol. C76, p. 055206, 2007.
- [32] N. Baillie *et al.*, “Measurement of the neutron F2 structure function via spectator tagging with CLAS,” *Phys.Rev.Lett.*, vol. 108, p. 142001, 2012.
- [33] M. Hattawy *et al.* (EG6 Working Group), “Deeply Virtual Compton Scattering off  $^4\text{He}$ ,” *CLAS internal analysis note*, 2016.
- [34] C. Ciofi degli Atti and B. Z. Kopeliovich, “Final state interaction in semi-inclusive DIS off nuclei,” *Eur. Phys. J.*, vol. A17, pp. 133–144, 2003.
- [35] C. Ciofi degli Atti, L. Kaptari, and B. Kopeliovich, “Final state interaction effects in semiinclusive DIS off the deuteron,” *Eur.Phys.J.*, vol. A19, pp. 145–151, 2004.
- [36] M. Alvioli, C. Ciofi degli Atti, and V. Palli, “Slow proton production in semi-inclusive DIS off nuclei: The Role of final state interaction,” *Nucl.Phys.*, vol. A782, pp. 175–178, 2007.
- [37] V. Palli *et al.*, “Slow Proton Production in Semi-Inclusive Deep Inelastic Scattering off Deuteron and Complex Nuclei: Hadronization and Final State Interaction Effects,” *Phys.Rev.*, vol. C80, p. 054610, 2009.
- [38] L. Frankfurt and M. Strikman, “Hard Nuclear Processes and Microscopic Nuclear Structure,” *Phys.Rept.*, vol. 160, pp. 235–427, 1988.
- [39] C. Ciofi degli Atti and S. Simula, “Slow proton production in semiinclusive deep inelastic lepton scattering off nuclei,” *Phys.Lett.*, vol. B319, pp. 23–28, 1993.
- [40] W. Melnitchouk, M. Sargsian, and M. I. Strikman, “Probing the origin of the EMC effect via tagged structure functions of the deuteron,” *Z. Phys.*, vol. A359, pp. 99–109, 1997.
- [41] C. Ciofi delgi Atti and L. Kaptari, “A Non factorized calculation of the process  $\text{He-3}(e, e\text{-prime } p) \text{H-2}$  at medium energies,” *Phys.Rev.Lett.*, vol. 100, p. 122301, 2008.

- [42] C. Ciofi degli Atti and L. Kaptari, “Semi-inclusive Deep Inelastic Scattering off Few-Nucleon Systems: Tagging the EMC Effect and Hadronization Mechanisms with Detection of Slow Recoiling Nuclei,” *Phys.Rev.*, vol. C83, p. 044602, 2011.
- [43] W. Melnitchouk, A. W. Schreiber, and A. W. Thomas, “Deep inelastic scattering from off-shell nucleons,” *Phys. Rev.*, vol. D49, pp. 1183–1198, 1994.
- [44] M. Amaryan *et al.*, “The Structure of the Free Neutron at Large x-Bjorken (PR12-06-113),” *A proposal to PAC 30*, 2006.
- [45] O. Hen *et al.*, “In Medium Nucleon Structure Functions, SRC, and the EMC effect (PR12-11-107),” *A proposal to PAC 38*, 2011.
- [46] O. Hen *et al.*, “In Medium Nucleon Structure Functions, SRC, and the EMC effect (PR12-11-003A),” *A run group proposal to PAC 43*, 2015.
- [47] A. Klimenko *et al.*, “Electron scattering from high-momentum neutrons in deuterium,” *Phys.Rev.*, vol. C73, p. 035212, 2006.
- [48] L. P. Kaptari, A. Del Dotto, E. Pace, G. Salme’, and S. Scopetta, “Distorted spin-dependent spectral function of an  $A=3$  nucleus and semi-inclusive deep inelastic scattering processes,” *Phys. Rev.*, vol. C89, no. 3, p. 035206, 2014.
- [49] K. A. Griffioen *et al.*, “Measurement of the EMC Effect in the Deuteron,” *Phys. Rev.*, vol. C92, no. 1, p. 015211, 2015.
- [50] H. Fenker *et al.*, “BoNus: Development and use of a radial TPC using cylindrical GEMs,” *Nucl. Instrum. Meth.*, vol. A592, pp. 273–286, 2008.
- [51] M. Sargsian and M. Strikman, “Model independent method for determination of the DIS structure of free neutron,” *Phys. Lett.*, vol. B639, pp. 223–231, 2006.
- [52] W. Cosyn, V. Guzey, M. Sargsian, M. Strikman, and C. Weiss, “Electron-deuteron DIS with spectator tagging at EIC: Development of theoretical framework,” *EPJ Web Conf.*, vol. 112, p. 01022, 2016.
- [53] S. J. Brodsky, I. Schmidt, and J.-J. Yang, “Nuclear antishadowing in neutrino deep inelastic scattering,” *Phys. Rev.*, vol. D70, p. 116003, 2004.
- [54] I. C. Cloet, W. Bentz, and A. W. Thomas, “Isovector EMC effect explains the NuTeV anomaly,” *Phys. Rev. Lett.*, vol. 102, p. 252301, 2009.
- [55] “CLAS12 Technical Design Report,” 2008.
- [56] J. Peyré, B. Genolini, and J. Poutas, “A Full-Scale Prototype for the Tracking Chambers of the ALICE Muon Spectrometer,” 1998.

- [57] T. Abe *et al.*, “Belle II Technical Design Report,” 2010.
- [58] E. Etzion *et al.*, “The Certification of ATLAS Thin Gap Chambers Produced in Israel and China,” 2004.
- [59] S. Biagi, “Monte Carlo simulation of electron drift and diffusion in counting gases under the influence of electric and magnetic fields,” *Nucl.Instrum.Meth.*, vol. A421, pp. 234–240, 1999.
- [60] M. Battaglieri *et al.*, “The Heavy Photon Search test detector,” *Nucl.Instrum.Meth.*, vol. A777, pp. 91–101, 2015.
- [61] T. C. Collaboration, “Clas12 forward tagger (ft) technical design report.” <https://www.jlab.org/Hall-B/clas12-web/docs/ft-tdr.2.0.pdf>, 2012. Online; accessed 29 January 2016.
- [62] K. Emi *et al.*, “Study of a  $dE/dx$  measurement and the gas-gain saturation by a prototype drift chamber for the BELLE-CDC,” *Nucl. Instrum. Meth.*, vol. A379, pp. 225–231, 1996.
- [63] R. B. Wiringa, V. Stoks, and R. Schiavilla, “An Accurate nucleon-nucleon potential with charge independence breaking,” *Phys.Rev.*, vol. C51, pp. 38–51, 1995.
- [64] B. S. Pudliner *et al.*, “Quantum Monte Carlo calculations of nuclei with  $A \leq 7$ ,” *Phys.Rev.*, vol. C56, pp. 1720–1750, 1997.
- [65] R. B. Wiringa , *Private communication*.
- [66] C. Ciofi degli Atti , *Private communication*.
- [67] W. Cosyn and M. Sargsian, “Final-state interactions in semi-inclusive deep inelastic scattering off the Deuteron,” *Phys. Rev.*, vol. C84, p. 014601, 2011.
- [68] K. Egian, L. Frankfurt, W. R. Greenberg, G. A. Miller, M. Sargsian, and M. Strikman, “Searching for color coherent effects at intermediate  $Q^2$  via double scattering processes,” *Nucl. Phys.*, vol. A580, pp. 365–382, 1994.
- [69] L. L. Frankfurt, W. R. Greenberg, G. A. Miller, M. M. Sargsian, and M. I. Strikman, “Color transparency effects in electron deuteron interactions at intermediate  $Q^2$ ,” *Z. Phys.*, vol. A352, pp. 97–113, 1995.